LBNL-47385

ERNEST ORLANDO LAWRENCE BERKELEY NATIONAL LABORATORY

A Novel Invasion Percolation Model for Co-Interpenetrating Composites

Tim Perham

Materials Sciences Division

December 2000

Ph.D. Thesis

REFERENCE COPY
Does Not
Circulate

Lawrence Berkeley National Laboratory
Annex

LBNL-47385
Copy 1

DISCLAIMER

This document was prepared as an account of work sponsored by the United States Government. While this document is believed to contain correct information, neither the United States Government nor any agency thereof, nor the Regents of the University of California, nor any of their employees, makes any warranty, express or implied, or assumes any legal responsibility for the accuracy, completeness, or usefulness of any information, apparatus, product, or process disclosed, or represents that its use would not infringe privately owned rights. Reference herein to any specific commercial product, process, or service by its trade name, trademark, manufacturer, or otherwise, does not necessarily constitute or imply its endorsement, recommendation, or favoring by the United States Government or any agency thereof, or the Regents of the University of California. The views and opinions of authors expressed herein do not necessarily state or reflect those of the United States Government or any agency thereof or the Regents of the University of California.

LBNL-47385

A Novel Invasion Percolation Model for Co-Interpenetrating Composites

Tim Perham
Ph.D. Thesis

Department of Materials Science and Engineering
University of California, Berkeley

and

Materials Sciences Division
Ernest Orlando Lawrence Berkeley National Laboratory
University of California
Berkeley, CA 94720

December 2000

This work was supported by the Director, Office of Science, Office of Basic Energy Sciences, Materials Sciences Division, of the U.S. Department of Energy under Contract No. DE-AC03-76SF00098.

A Novel Invasion Percolation Model for Co-Interpenetrating Composites

by

Timothy James Perham

B.S. (University of Arizona) 1990
M.S. (University of California, Berkeley) 1996

A dissertation submitted in partial satisfaction of the

requirements for the degree of

Doctor of Philosophy
in

Engineering-Materials Science and Mineral Engineering

in the

GRADUATE DIVISION

of the

UNIVERSITY OF CALIFORNIA, BERKELEY

Committee in charge:

Professor Lutgard C. De Jonghe, Chair
Professor Daryl C. Chrzan
Professor Nathan W. Cheung

Fall 2000

Abstract

A Novel Invasion Percolation Model for Co-Interpenetrating Composites

by

Timothy James Perham

Doctor of Philosophy in Materials Science and Engineering

University of California, Berkeley

Professor Lutgard C. De Jonghe, Chair

A novel Invasion Percolation model for simulating the reactive metal infiltration of ceramics to form a co-interpenetrating composite is presented. By combining the pore-level dynamics of percolation models with kinetic Monte Carlo methods for simulating surface phase transformation it is possible to simulate both thermodynamic driving forces for infiltration: the applied pressure and the reactive wetting process. In doing so the model describes both the capillary fingering effects that dominate at high pressures and the time evolution of reaction byproduct phases that cause pore space closure at high temperature. At very high temperature and/or low pressure a "core-shell" morphology forms. At very high pressures the assumption of quasi-static flow in discrete pore throats is violated, and viscous channel flow occurs that leaves undesirable levels of residual porosity.

Statistics derived from percolation theory were applied to determine the effective percolation threshold pressure for infiltration and the critical pressure for divergence of the fingerwidth. At pressure intermediate between these two extremes the residual pore size distribution was found to determine the probability of discrete pore cluster

occurrence, which served as a means, in addition to fingerwidth, for quantifying microstructures. This enabled the application of Weibull statistics to determine the 98 % probability survival strength and the Weibull shape factor. For analyzing mechanical properties, the pore cluster probability is a better measurement. For analysis of thermal properties, the fingerwidth should be used.

The adjustable parameters experimented with were the transformation rate, initial transformation contact angle, applied pressure, kinetic growth rate constant, and initial matrix porosity. The Aluminum/Silicon Carbide system was chosen first because of the large volume of wetting data available, but the model is designed to simulate any system were reactive wetting data, kinetic growth rate data, and correlation of surface XRD data with temperature are available. In general, the conditions most favorable for the formation of the most interconnected composites were high transformation rate, low to intermediate pressure, low initial transformation contact angle (low temperature), low kinetic growth rate constant, and low initial matrix porosity. The optimal combinations were presented in the form of Weibull survival probability plots and process maps.

TABLE OF CONTENTS

Chapter One *Introduction*

1 Introduction 1
2 Background: Flow Regimes in Fluids 4
3 Pore Level Models 6

3.1 Non-wetting Invasion 7
3.2 Wetting Invasion 8

4 Objectives 9

Chapter Two *Classical Invasion Percolation*

1 Introduction 11
2 Thermodynamics 11

2.1 Flow Potential 11
2.2 Capillary Length 13
2.3 Wetting and Non-wetting invasion of single pores 15

3 Experimental Determination of Capillary Length Criterion 16
4 Simulation Technique 19

4.1 Determination of Interface Position 19
4.2 Interface Growth Algorithm 21
4.3 Statistical Interpretation of Results 22

5 Construction of Computer Model 23
6 Initial Simulation Results 24

6.1 Periodic Boundary Conditions 24
6.2 Divergence of Fingerwidth 26

7 Conclusion 29

Chapter Three *Invasion Percolation Model With Reaction Kinetics*

1 Introduction: Real Microstructures 31
2 Interface Transformation Dynamics 33

2.1 Transformation Rate 33
2.2 Transformation Time Intervals 35

3 Product Phase Growth 36

3.1 Growth Rate Constant 36
3.2 Simulation of Core-Shell Effect 37

4 Initial Simulation Results 38

4.1 Chemical Reaction Regime 39
4.2 Infiltration Regime 40

5 Quantification of Results 41

5.1 Divergence of the Fingerwidth 41
5.2 Process Mapping 42
5.3 Residual Pore Size Distribution and Mechanical Properties 43

5.3.1 Determination of Residual Pore Size Distribution 43
5.3.2 Pore Cluster Probability 44
5.3.3 Mechanical Properties 46

6 Experimental Plan 47

6.1 Model Systems 47
6.2 Incompressible Phase Assumption 48

7 Random Numbers in Simulation 49

Chapter Four *Baseline Simulation*

1 Lattice Initial Conditions 51
2 Microstructure 52
3 Data Reduction 53
4 Pore Cluster Probability and Weibull Survival Probability 55
5 Summary 61

Chapter Five *Invasion Percolation with Interface Transformation*

1 Introduction 63
2 Application of Transformation Rate 63
3 *Lattice I* Simulations 65

3.1 Rapid Transformation Rate, High Kinetic Growth Rate Constant, with Trapping 65
3.2 Modifying θ_i 68
3.3 Modifying the Rate R 70
3.4 Modifying the Kinetic Growth Rate Constant k 72
3.5 Simulations Without Trapping Mechanism 73

4 *Lattice II* Simulations 75

4.1 Low Temperature, without Trapping 76
4.2 High Temperature, without Trapping 77
4.3 Low Temperature, with I/P Trapping Mechanism 78

5 Process Maps 79

5.1 Low Temperature Transformation, with Trapping 80
5.2 High Temperature Transformation, with Trapping 81
5.3 Low Temperature Transformation, without Trapping 81
5.4 Low Temperature Transformation without Trapping, *Lattice II* 83
5.5 Effect of Processing Temperature 84
5.6 Effect of Initial Matrix Porosity 85

Chapter Six *Discussion*

1 Adjustable Parameters 89
2 Primary Effects 90

2.1 Applied Pressure 90
2.2 Transformation Rate 90
2.3 Initial Transformation Contact Angle 91
2.4 Kinetic Growth Rate Constant 92
2.5 Initial Matrix Porosity 92
2.6 Invasion Percolation Trapping Mechanism 93

Chapter Seven *Concluding Remarks*

1 Physical Limitations of the Model 94

1.1 Permeability 94
1.2 Dimensional Dependence of Properties 95
1.3 Mechanical Properties 96
1.4 Random Number Generation and Precision 96

2 Application of Scaling Laws 97
3 Algorithm Development 98
4 Physical versus Phenomenological Models 98

Appendices

Appendix One Catalogue of Invasion Percolation Interactions 100
Appendix Two Mechanism for Overlaying Data Structures 102
Appendix Three Main Simulation Flowchart 103
Appendix Four Derivation of Weibull Survival Probability 104

Chapter One Introduction

1 Introduction

One of the dominant themes in materials science today is the fabrication of unique composite materials that combine the advantageous properties of dissimilar materials. In the processing of composites, it is typically quite difficult to distribute the secondary phase uniformly in anything but dilute concentrations. Efforts at increasing the volume fraction of secondary phase are often limited by clustering or aggregation, which can lead to a non-homogeneous microstructure. For this reason, materials were sought in which the two phases are co-interpenetrating, i.e. each phase spans or percolates through the microstructure entirely so that a large volume fraction of an interconnected secondary phase is possible.

An example of such materials are co-interpenetrating ceramic metal composites, which are useful materials in that they can incorporate large volume fractions of metal phase and can be processed with *near-net shape* geometries, which eliminates the need for costly machining and finishing operations. Their useful properties include high specific stiffness, toughness, wear resistance, and the ability to tailor the thermal conductivity and coefficient of thermal expansion by controlling the volume fraction of metal. These materials and related processes currently find application as semiconductor packaging materials, and in the hermetic sealing of silicon carbide (SiC) tubes to SiC composite plates. Research is ongoing for their application in aerospace structures, armor plating, automobile components, and locomotive brake pads.[1]

Up to now the understanding of melt infiltration processing of composites has been entirely empirical and specific to the material system of interest. With the proper

processing conditions and choice of materials, spontaneous (pressureless) infiltration of porous ceramic bodies with liquid metals has been achieved.[2,3,4,5] Ceramic-matrix composites (CMC's) have also been successfully fabricated using pressurized infiltration with a solution precursor.[6] The primary goal of this research is to develop a modeling system that enables the identification of the critical processing and material parameters that relate directly to the properties of the composite through the resulting structure. For most cases a fully infiltrated, void-free, highly interconnected microstructure is desirable.

It is known that the processing times in the fabrication of these materials must be minimized to prevent the formation of high volume fractions of reaction product phases, which would be detrimental to the properties of the composite. The two main process controls for achieving this are pressure and temperature. At high pressure, the infiltration rate increases in response to viscous forces, but at the same time the occurrence of capillary fingering increases, which can lead to residual porosity. This capillary fingering phenomenon occurs as a result of the fluid invasion pattern following a path of least resistance in the porous medium defined by the largest pore openings, where the resisting capillary pressure is the lowest. At high temperature, the surface reaction kinetics are accelerated, which increases the infiltration rate, but the growth rate of secondary phases in the pore space is also increased, which leads to a reduction in permeability and a slowing of the rate. A "core-shell morphology" results as a fully reacted shell of high molar volume phases seals an unreacted core from the fluid source.

The reactive infiltration process operates on two levels. On the pore level, the so-called reactive wetting process provides the thermodynamic driving force when the apparent contact angle θ, which the liquid metal makes with the solid ceramic, changes in

response to the physical state of the surface. Complex effects such as the reduction of surface oxides, capillary condensation ahead of the fluid front, and alloy formation contribute to the observed reduction in θ over time, causing a capillary rise-type effect. While this pore-level effect helps drive the infiltration, the associated product phase formation in the pore space acts to slow the rate and leads to trapped porosity by plugging pore throats and limiting the supply of reactive metal to the infiltration front. Furthermore, volumetric changes associated with this product phase, exotherms, and temperature-dependent reaction kinetics render the pore level effects operating at the interface very difficult to model.[7] On the continuum level, viscous drag to the infiltration front has been observed to slow the rate of infiltration over time. These losses occur by shear mechanisms within the pore throats (dominant for small pore throats), and by internal frictional losses within the fluid interior (dominant for the larger pore bodies). An accurate predicative model of how reactive infiltration will proceed to completion has remained elusive, due to the complex interplay between these pore-level and continuum-level effects.

Assuming a green compact or loose powder pack to be equivalent to a bundle of parallel capillaries, Washburn[8] derived an expression for the penetration depth, x, in a non-reactive infiltration process, in terms of the infiltration time, t, viscosity, μ, wetting angle, θ, surface tension, γ, and capillary diameter, D

$$x^2 = \gamma D t \cdot \cos\left(\frac{\theta}{4\mu}\right) \tag{1}$$

This expression, arrived at using the Hagen Poiseuille equation for capillary flow in straight cylinders, does not take into account local heterogeneities present in real porous

materials, and so underestimates the time required for complete infiltration. In practice, infiltration times are observed to be 10 to 20 times longer than what is predicted by the Washburn model. In addition, the effects due to surface reaction kinetics are ignored. More importantly, no means for predicting trapped porosity or a non-interconnected final microstructure exists in continuum models such as this.

2 Background: Flow Regimes in Fluids

Before the dynamic effects due to surface reaction kinetics can be understood, the basic fluid flow problem in non-reactive porous media must be considered. Fluid flow is described by the Navier-Stokes equation; the x-component equation is,

$$\rho\left(\frac{\partial V_x}{\partial t}+V_x\frac{\partial V_x}{\partial x}+V_y\frac{\partial V_x}{\partial y}+V_z\frac{\partial V_x}{\partial z}\right)=-\frac{\partial P}{\partial x}+\mu\left(\frac{\partial^2 V_x}{\partial x^2}+\frac{\partial^2 V_x}{\partial y^2}+\frac{\partial^2 V_x}{\partial z^2}\right)+\rho g_x \qquad (2)$$

where ρ is the fluid density, μ is the fluid viscosity, V_x, V_y, and V_z are the components of the fluid velocity, P is the applied pressure, g_x is the x-direction component of the gravitational force, and t is the time. For creeping flow in porous media, the Reynolds number is much less than one, and the inertial terms in the Navier-Stokes equation are negligible compared to gravity and the viscous pressure gradient.[9] For water percolating through sand, e.g., the velocity in the pore interstices (interstitial velocity) is less than 1 cm/s in creeping flow. For a complete solution to the creeping flow problem in porous media, a complete characterization of the pore space and complete solution to the viscous pressure field at all points in the medium is required, followed by integration of the velocity for each section of interface. For this reason, the empirically established models for estimating the extent of infiltration in porous media have relied on a volume-averaged

creeping flow equation known as Darcy's Law,[10] which assumes the form of the diffusion equation for momentum flux, and describes viscous pressure controlled flow:

$$u = -\frac{k}{\mu}\nabla(\rho\varphi) \tag{3}$$

Here u is the interstitial velocity, k the permeability (a geometry dependent quantity), μ the fluid viscosity, ρ the fluid density, and ϕ the potential field. The potential field may have competing components due to gravity, capillary pressure, applied viscous pressure, and hydrostatic pressure. In the case of water filtration through sand packs, for which the expression was originally derived, Darcy's Law assumes the form,

$$u = -\frac{k}{\mu}(\nabla P - \rho g) \tag{4}$$

where ∇P is the measured pressure gradient between the top and bottom of the column. Geometric models for the pore space permeability, k, assume volume averaged values for the porosity Φ and grain surface/volume ratio S, e.g. the well-know Carman-Kozeny equation,[11,12]

$$k = \frac{\Phi^3}{5S^2(1-\Phi)^2}. \tag{5}$$

These aforementioned expressions are mean field approximations that inadequately describe local effects which give rise to flow instabilities, and in the case of melt infiltration composites, undesirable heterogeneities in the resulting microstructure.

3 Pore Level Models

To account for these effects, pore-level models have been developed in which flow is described as an interface advancing in each pore throat nearly instantaneously between nearly stable configurations in response to discrete phenomena. In this idealization, termed "quasi-static flow", no viscous drag component is required as long as a sufficient fluid source to the advancing front exists. Thus pore-level models diverge from continuum models in that viscous pressure drops are neglected in the limit of vanishing flow rate. Two main pore level modes have been identified. In drainage, a wetting fluid is displaced (forced) from the medium, and the path of least resistance resides in the widest pore throats, where the capillary pressure is the lowest. Hence the capillary pressure opposes the fluid's movement. In imbibition, a non-wetting fluid is displaced instantaneously, and the path of least resistance resides in the narrowest pore throats, where the capillary pressure is the highest. So the capillary pressure helps drive the fluid in that case. It follows that the proposed approach for simulating melt infiltration is a hybrid model that incorporates both effects.

To understand fully the flow patterns that will develop in a porous medium, one must understand the interplay between the macroscopic viscous pressure gradient that enters Darcy's Law, and the microscopic capillary pressure that exists across fluid menisci in small pores. These forces are competing, and lead to a problem that can best be described as Invasion Percolation in a stabilizing gradient. The length scale over which the viscous pressure gradient becomes appreciable, in comparison to the capillary pressure, is called the capillary length. The capillary length defines the length scale over which the dominant flow patterns of the system are governed. This can be illustrated by

examining the effects observed in two-phase systems and drawing an analogy with the reaction-infiltration systems studied in this work.

3.1 Non-wetting Invasion

Experimental observations of flow in porous media have focused on two-phase flow, where the invading fluid is displacing another fluid phase already residing in the pore space (e.g. water displacing oil). These studies have shown that during non-wetting invasion (drainage), the interface is unstable and ramified viscous fingers will be present at length scales larger than the capillary length. When the invading fluid is less viscous than the displaced fluid ($\mu_i/\mu_d < 1$), the pressure is dropped in the displaced fluid ahead of the invasion front.[13,14] The capillary length defines the minimum spatial extent of the spacing between viscous fingers, and fractal viscous fingering patterns result. At length scales below the capillary length, Invasion Percolation trapping mechanisms leave behind enclosed loops of an incompressible phase, which is of paramount concern in the recovery of oil from a reservoir. In reaction-infiltration, however, the invading fluid is more viscous than the displaced fluid (a gas or vacuum), and therefore the pressure is dropped in the invading fluid behind the interface. This scenario most closely corresponds to using an applied pressure to drive flow before the surface energy effects contribute significantly to the driving force. Viscous fingering patterns resultant in this flow regime will follow an Invasion Percolation path in the largest available pore openings. The flow instabilities during this type of invasion will be present at length scales on the order of the capillary length, where the finger width is defined as the width of the finger itself, and not the finger spacing width as in the case of two-phase flow. The resulting flow pattern can be termed "channel flow." The entrapped phase enclosed by

the invading fluid is in this case a gas, which is to a certain degree compressible. To account for this disparity each enclosed interface loop must be reevaluated for possible new invasion sites after each pressure increment in a Monte Carlo percolation simulation.

3.2 Wetting Invasion

In experimental observations of wetting invasion (with $\mu_i/\mu_d < 1$) in two-phase flow, the resulting viscous fingers are compact in nature, since no trapping will occur at length scales less than the capillary length. The fingerwidth is defined as the spacing in the more viscous phase between the unstable flow patterns in the less viscous phase. In the reaction-infiltration model being discussed here, however, viscous imbibition[15,16] occurs, i.e. the invading fluid is more viscous than the displaced fluid ($\mu_i/\mu_d > 1$). Hence the pressure is dropped in the invading fluid behind the infiltration front. If the process is conducted at atmospheric pressure or in vacuum, the capillary forces alone comprise the infiltration driving force, so the dynamics of the process is wholly determined at the pore level. Interface roughening caused by fluctuations in the capillary pressure due to the random pore sizes exists, but is suppressed by the viscous pressure drop in the medium. Thus the capillary length (L_{cap}) in this instance represents an approximate estimate of the maximum extent of these roughened zones. Alternatively, one could say that the capillary pressure, in the local sense, sets the upper bound for the viscous pressure drop in the vicinity of the pore throat.

$$P_{cap} \geq L_{cap} \nabla P_{visc} \tag{6}$$

While in drainage the capillary length defines the length scale over which the viscous pressure gradient overwhelms capillary pressure to drive flow, in viscous imbibition (wetting invasion) the capillary length represents the length scale over which the viscous

drag on the interface becomes significant compared to the capillary pressure. At length scales approaching this capillary length, viscous forces tend to stabilize and "even out" the rough interface by presenting a drag to the supply of fluid to the invading front. The ratio of viscous to capillary forces is expressed in the capillary number

$$Ca = v\mu/\gamma \tag{7}$$

where v is the velocity, μ the viscosity, and γ the interfacial tension. This indicates that higher viscosities and velocities favor viscosity controlled flow, leading to channel flow in this model. In creeping flow regimes (very low capillary numbers), the assumption of quasi-static flow permits the use of percolation models in the description of pore-level determined processes.

4 Objectives

The goal of this work is to create a predictive computer model for the processing of co-interpenetrating composites through a reactive metal infiltration route. In doing so, the model seeks to reveal the interrelationships between the processing conditions, of pressure, temperature, and time, and the resultant microstructure and mechanical properties. A novel Invasion/Percolation model is developed which uses kinetic Monte Carlo methods to simulate the effect of the interface transformation rate. The additional thermodynamic driving force, apparent in the reactive wetting process, is dynamically linked to the product phase formation in the pore space that could seal off the infiltration core from the reactive metal species.

Using statistics derived from percolation theory, the threshold values of the critical parameters (pressure, interface transformation rate, and system size) are sought that create the optimal microstructure. In most cases the desired structure is a fully

interconnected composite with zero residual porosity and minimal interfacial reaction byproduct, containing the optimal metal concentration to yield the desired properties. The effects of system dependent material parameters, such as the composition of the metal alloy, the porous ceramic preform, and surface wetting agents, are included in the model in the interface reaction rate between the metal and ceramic.

---

[1] Clarke, D.R., "Interpenetrating Phase Composites", *J. Am. Ceram. Soc.*, **75** [4] 739-59 (1992).
[2] Aghajanian, M.K., Buirke, J.T., White, D.R., and Nagelberg, A.S., *Proc. Int. SAMPE Symp.* **34** (1989) 817.
[3] Xiao, M.X., and Xiao, F.Y., "Spontaneous Infiltration of Aluminum-Silicon Alloy into Silicon Carbide Preforms in Air", *J. Am. Ceram. Soc.*, **79** 1 102-08 (1996).
[4] Cornie, J.A., Chiang, Y., Uhlmann, D.R., Mortensen, A., and Collins, J.M., "Processing of Metal and Ceramic Matrix Composites", *Am. Ceram. Soc. Bull.* **65** 2 293-304 (1986).
[5] Hillig, W.B., "Making Ceramic Composites by Melt Infiltration", *Am. Ceram. Soc. Bull.* **73** 4 56-62 (1994).
[6] Lange, Tu, and Evans, *Mat. Sci. Eng. A* **195** (1995).
[7] Hillig, W.B., "Melt Infiltration Approach to Ceramic Matrix Composites," *Am. Ceram. Soc. Bull.* **71** 2 C56-62 (1988).
[8] Washburn, E.W., "The Dynamics of Capillary Flow," *Phys. Rev.*, **17** 273-83 (1921).
[9] Bird, R.B., Stewart, W.E., and Lightfoot, E.N., p. 57 in *Transport Phenomena*, John Wiley and Sons, New York, NY, 1960.
[10] Darcy, Henry, *Les Fontaines Publiques de la Ville de Dijon*, Victor Dalmont, Paris (1856).
[11] Carman, P.C., *Trans. Inst. Chem. Eng. London* **15,** 150 (1937).
[12] Kozeny, J., Royal Academy of Science, Vienna, Proc. Class I **136,** 271 (1927).
[13] Lenormand, R., Touboul, E. , and Zarcone, C., *J. Fluid Mech.* **189** 165 (1988).
[14] Wong, P-z., "Flow in Porous Media: Permeability and Displacement Patterns", *Mat. Res. Soc. Bull.* **5** 34-37 (1994).
[15] He, S., Galathara, L., Kahanda, M. K. S., and Wong, P-z., "Roughness of Wetting Invasion Fronts in Porous Media," *Phys. Rev. Lett.* **69** 26 3731 (1992).
[16] Martys, N., Cieplak, M., and Robbins, M. O., "Critical Phenomena in Fluid Invasion of Porous Media," *Phys. Rev. Lett.* **66** 8 1058 (1991).

Chapter Two Classical Invasion Percolation

1 Introduction

The percolation theory was invented in 1957,[1] and modeling techniques were subsequently developed for simulating the immiscible displacement of one fluid by another under the action of capillary forces in a disordered pore network.[2] In this method the porous medium is represented by some kind of lattice structure, and a random number assigned to each site (or bond) to represent the pressure at which it will fill with the displacing fluid. At each time-step the fluid configuration grows by occupying the accessible site with the smallest (for drainage) or largest (for imbibition) random number. The process ends when the lattice is spanned by the invading phase. Regions of displaced incompressible phase that become disconnected from the outlet are "trapped" and cannot be invaded. In the petroleum industry, this has corresponded physically to crude oil globules, which become isolated in the pore space and are irretrievable. Invasion Percolation[3,4,5] differs from classical site or bond percolation in that only accessible sites adjacent to the fluid interface are allowed to fill. The pressure (simulated by the interface curvature in a pore) is increased incrementally until the first unstable meniscus is found, and the interface is allowed to equilibrate at that value of the pressure. The pressure at which the lattice is spanned is called the threshold pressure, P_c.

2 Thermodynamics

2.1 Flow Potential

One can associate a change in potential energy in a system with the action of a field of forces alone, provided that the forces are conservative in nature, i.e., the work

done on the system by the forces depends only on the initial and final states, and not the path taken. Such systems are capable of storing energy merely from the configuration of the system itself. In the flow described in this work, these conditions are met if the flow is irrotational, where the curl of the force field is zero

$$\nabla \times F = 0 \tag{1}$$

where F represents the total force field acting on the fluid mass. Physically this condition is met if the fluid is of constant density, implying constant composition, and no thermal gradient exists that would cause significant convection currents.[6] Under these conditions a scalar flow potential field can be defined which incorporates all the relevant thermodynamic driving forces in the system, for instance

$$\phi = \frac{P_{cap}}{\rho} + \frac{P_{applied}}{\rho} - gz \tag{2}$$

where P_{cap} is the capillary pressure (assumed positive for wetting systems), $P_{applied}$ the applied viscous pressure, and z the hydraulic head. The gradient of this potential constitutes the thermodynamic driving force per unit mass. Darcy's Law provides a continuum approximation for the average interstitial velocity as a function of the volume-averaged quantities of pore space permeability, fluid viscosity, and the potential field.

Models like Invasion Percolation were developed to describe pore level effects such as capillary fingering and localized residual porosity, which are not described by Darcy's Law. In these models, flow is described as an interface advancing through the lattice element of least resistance between nearly stable configurations. Viscous pressure and drag effects, which are essential to continuum models, are neglected in the limit of zero flow. The fluid relaxation time between successive pore level events is considered negligible in comparison to the speed at which the pore fills, provided that the magnitude

of the capillary forces is much greater than the viscous dissipative forces. In quasi-static displacement, the interface configuration can be determined through the solution of the Young-Laplace equation

$$P_{cap} = \gamma \cos\theta \left[\frac{1}{r_1} + \frac{1}{r_2} \right] \tag{3}$$

where γ is the liquid surface tension, θ is the liquid/solid contact angle, and r_1 and r_2 are the principal radii of curvature of the fluid interface.

2.2 Capillary Length

The capillary length, L_{cap}, is defined as the length scale over which the viscous forces become comparable to the capillary forces. If the system size is smaller than the capillary length, a pore level determined process can be assumed and therefore quasi-static flow. At the crossover point, when the magnitudes are comparable, for a given cross sectional area of flow,

$$L_{cap} \Delta P_{visc} = R P_{cap} \tag{4}$$

where R is the length of the pore throat. Assuming flow to pass through N such pore/throat bodies per unit area, Koplik, *et al.* defined the capillary length criterion as

$$L_{cap} = RK / Ca \tag{5}$$

where K is a function of the pore throat-to-pore body radius ratio and the porosity, and Ca is the capillary number.[7]

If the sample size exceeds the capillary length, some method for calculating the total viscous pressure drop in the porous media is needed. By summing a sufficiently high number of self-avoiding random paths through the lattice to the interface, while

calculating the viscous pressure drop for each, then averaging over all walks arriving at a particular point on the interface, an average viscous pressure drop to that point could be obtained. This method presumes statistical independence of each walk, i.e., the pore space is uniform enough to rule out large local areas of reduced permeability. In a non self-avoiding walk, for a 100 X 100 lattice, with only 2 choices for each step in the walk, 2^{100} possible walks exist, ~ 10^{30}, a very large number; so it remains to be seen if the method is feasible using the computational resources available. This method also assumes that no single main hydraulic "pipeline" forms which channels most of the flow, i.e. some viscous shear component in smaller pore throats is present. Hence the fluid is idealized as sampling all the pore space en route to the interface, a good approximation for creeping flow problems.

Once an average viscous pressure drop is obtained, the rate of rise of a liquid meniscus in a pore throat can be obtained using the Washburn equation[8]

$$\frac{dh}{dt} = \frac{1}{8\mu h}\left[\Delta P - \rho g h\right] r_0^{\,2} \qquad (6)$$

where h is the height above a reference level, μ and ρ are the fluid viscosity and density, ΔP is the capillary pressure across the meniscus, and r_0 is the effective capillary radius, sometimes termed the "hydraulic radius".[9] This radius is sometimes expressed as the total empty pore volume to wetted surface area ratio, and can also be expressed in terms of the porosity, ϕ,

$$R = \frac{\phi}{a_v(1-\phi)} \qquad (7)$$

with a_v the internal surface to volume ratio of the medium. The driving force in the Washburn equation is the difference between the capillary pressure and the hydrostatic

head. This expression can be equated to the viscous pressure drop in a medium being invaded from below. Therefore, if the surface transformation kinetics decrease the apparent contact angle in the pore capillary at a rate exceeding the meniscus velocity as determined by the Washburn equation, contact line pinning would occur, distorting the meniscus while the fluid in the pore space fully relaxed. Also, a large enough hydrostatic pressure would eventually stop the meniscus advance (in non overpressurized flow) and the infiltration would cease.

In small laboratory-sized samples and the small composite parts envisioned produced by the melt infiltration technique, the capillary length would exceed the sample size, rendering the effects of viscous pressure drops negligible. Nevertheless, the infiltration may be stopped with the formation of a "core-shell" morphology, in which a larger molar volume product phase forms at the periphery, which seals the core from the fluid source. Thus one of the goals of this work is to determine what temperatures and applied pressures are optimal for forming fully interconnected composites with minimal interfacial reaction byproduct.

2.3 Wetting and Non-wetting invasion of single pores

Imbibition and drainage in a single pore is simply illustrated in Figure 1, in which the direction of the Hagen-Poiseuille flow through a cylindrical pore throat/body combo,

$$Q = \frac{\pi r^4}{8d\mu}\left(P_{nw} - P_w - P_{cap}\right) \tag{8}$$

indicates the wetting or non-wetting nature of the process. For positive flowrate from left to right, during drainage, the inequality $P_{nw} - P_w > P_{cap}$ holds. This inequality is most easily met when the capillary pressure, defined in cylindrical pore throats as P_{cap} =

$2\gamma\cos\theta/r$, is smallest, which occurs in the pores of largest throat radii. Consequently the path of least resistance for the fluid during drainage will reside in the largest pores. Conversely, during imbibition, the inequality $P_{nw} - P_w < P_{cap}$ holds, which is most easily met when the capillary pressure is largest, in pores of smallest throat radii. In that case the path of least resistance will reside in the smallest pores. Thus, during drainage the capillary pressure resists forward displacement, while in imbibition it assists it.

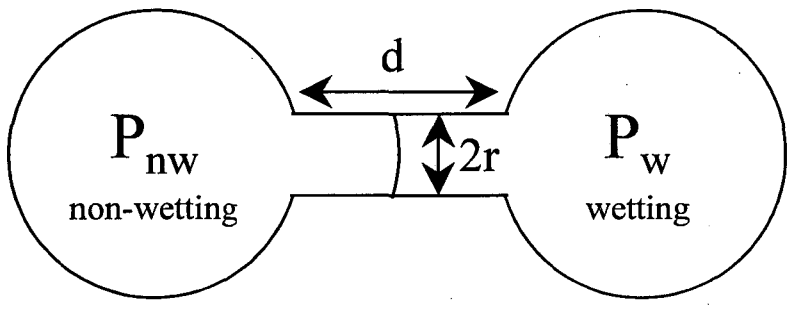

Figure 1 Pore throat/body combo with fluid meniscus to illustrate the wetting or non-wetting nature of displacement through single pores.

3 Experimental Determination of Capillary Length Criterion

Ceramic matrix materials were sought that would enable the most precise control of matrix porosity prior to infiltration. An amorphous Silicon Carbide (SiC) ceramic material was prepared by curing a SiC polymer precursor, Allylhydridopolycarbosilane (AHPCS).[i] The porosity in these materials can be controlled with the curing rate of the polymer, and they will consolidate with little or no shrinkage, thus the preform can be machined to near net shape before subsequent curing and infiltration. Attempts to use the

[i] Starfire Systems; Watervliet, NY

precursor Polydimethylsilane proved ineffective due to excessive weight loss during the curing process, conducted without an autoclave.

Assuming 60-65% yield by weight, AHPCS was mixed with SiC powder[ii] in hexane with a dispersant[iii] using an ultrasonic probe. When mixed at the proper proportions, the resulting composite preform was nearly non-porous in the green state. The solution was stir dried to a high viscosity and then poured into a steel die to dry. Upon removal the material was pressed at 5 MPa and 1 gram pellets placed in a graphite element furnace for pyrolysis. 62% yield to amorphous SiC was obtained by curing at 1100°C for 2 hours in 3 psig Argon. The ramp rate to peak temperature was 1.25°C /minute, and the cooling rate was 8°C /minute. A very fine network pore structure for metal infiltration was produced by the volatilization of low molecular weight organics during the conversion process to SiC. Based on the weight loss observed, the approximate porosity of the composite ceramic obtained was between 15 and 25%.

The porous composite preforms were infiltrated with an Al/20Si alloy at 1350°C for 1.5 hours in a tungsten element furnace at 2 psig He. The maximum extent of the infiltration was measured and the creeping flow rate determined to be 0.4 μm/second. SEM cross-sections such as the one shown in Figure 2 showed pore throat/pore body ratios ranging from 1/3 to 1/10. Using a mean pore body size of 5.2 μm obtained from the SEM Table 1 was constructed using the analysis of Koplik *et al.*[7] The table clearly

---

[ii] H.C. Starck; Berlin, Germany

[iii] BRIJ-35, Aldrich Chemical Company; Milwaukee, WI

demonstrates the capillary-dominated flow regime required for the assumption of quasi-static flow in systems of this size.

Infiltration velocity (μm/s)	Porosity	Pore Body Radius (μm)	Capillary Length (cm)	L_{cap}/size
0.4	0.15	5.2	1.1	3
0.4	0.15	5.2	9.0	20
0.4	0.25	5.2	14.2	35
0.4	0.15	5.2	39.0	100
0.4	0.25	5.2	65.0	160

Table 1 Results for experimental determination of capillary length in SiC/Al-20Si system.

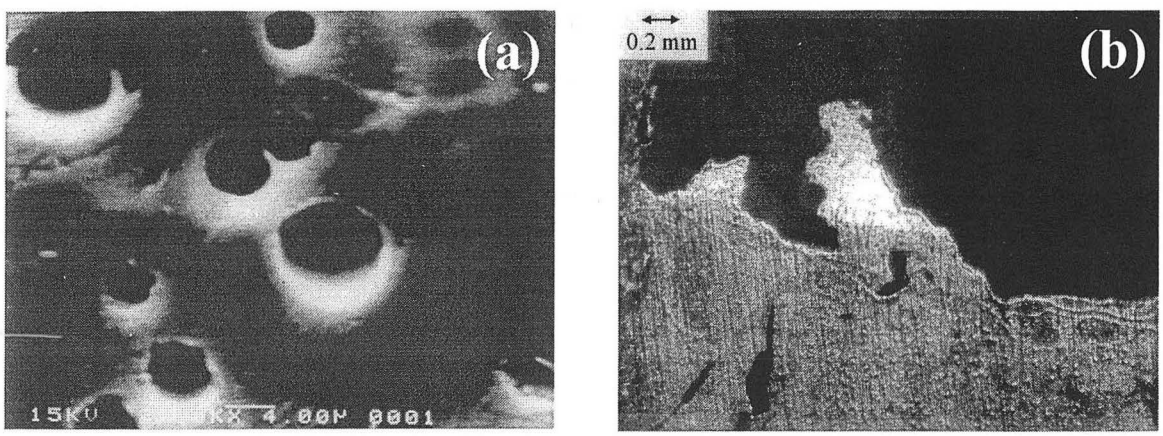

Figure 2 SEM cross section of amorphous SiC ceramic composite preform prepared by pyrolysis of AHPCS showing dominant pore bodies and throats, (a); and composite preform infiltrated with Al-20Si alloy for experimental verification of the capillary length criterion, (b).

4 Simulation Technique

4.1 Determination of interface position

In Invasion Percolation, like other "front tracking" techniques, the exact interface position and pore status are computed and stored at all times during the simulation. A dual honeycomb lattice of disks and pores is established, with randomness injected into the model in the lattice site radii and interface transformation times. A lattice with disks of equal radii would simulate a perfectly homogenous pore space. The closest physical analog to the model is a parallel array of cylindrical rods, with no rod overlap, so at some point this approximation must be considered when attempting to relate results to real 3-D systems (the increased connectivity of a 3-D system would enhance the cooperative fluid advance mentioned below). The complexity of the interface growth process makes such assumptions necessary, as a finite difference solution to 5 transcendental equations is required to define the position of a meniscus contacting 2 disks (Fig. 3).[10]

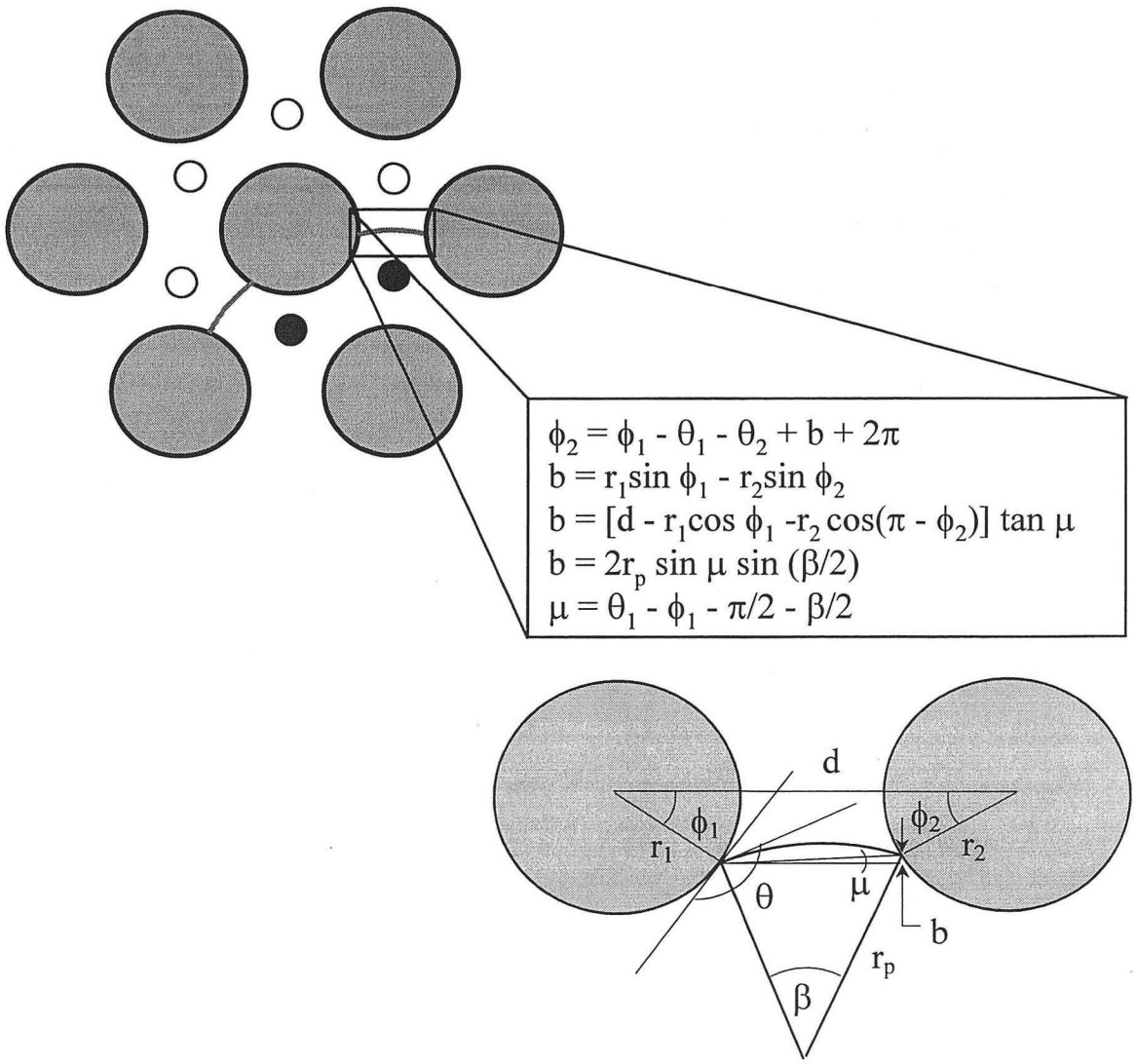

Figure 3 The solution to the 2-D interface problem on the dual honeycomb lattice consists of the simultaneous solution to a set of transcendental equations using a finite difference routine.

To set the parameters in the finite difference algorithm, the liquid/solid contact angle is set constant, and the initial interface curvature for a given applied pressure is set according to the Young-LaPlace relation $\Delta P = \gamma cos\theta/r$, where ΔP is the simulated pressure, r is the radius of curvature, and γ is the fluid surface tension. The non-

uniformity of the pore space is determined by the range of lattice disk radii allowed, simulating actual grain size/pore size ratios in porous ceramic bodies.

4.2 Interface Growth Algorithm

After solving for the interface position, an algorithm is called that allows the interface to advance according to a hierarchical set of rules. Individual menisci are unstable when they intersect adjacent disks making up the lattice ("touches"), intersect adjacent menisci in the pore space ("overlaps"), and when no stable meniscus can be found at the current geometric configuration ("bursts"). The overlap instability is the most common interaction in wetting invasion, leading to cooperative fluid advance with little or no pore space trapping. Herein lies the difference between Invasion Percolation and classical percolation models. The actual geometric configuration of the interface is not computed in classical percolation; those models in general only describe the "burst" advance of unstable menisci, which is independent of the current interface and local lattice configuration. Incorporation of "touch" and "overlap" interactions within the lattice topology leads to large changes in the resultant growth morphology.

In this Invasion Percolation (IP) model the interface configuration equilibrates according to an hierarchical scheme in which independent (non-interactive) stabilities are removed first by replacing the initial unstable meniscus with two new ones, each connected to the newly activated section of lattice, and at the initial value of the contact angle θ. Interacting stabilities, which appear through cooperative fluid advance mechanisms, are removed next by forming a single new meniscus from the original intersecting menisci. As new menisci are created, they are tested for stability against the aforementioned interactions. Any new instabilities are not removed until the remainder

of the active interface is traversed, and preexisting instabilities removed. When a new section of interface intersects a non-adjacent section, a flag is set and an enclosed loop is formed around the entrapped section of lattice. Periodic boundary conditions are employed to increase the statistical significance of the results by removing edge effects. Thus, an arc on the interface (an individual mensiscus) on one edge of the lattice samples the lattice on the other edge during the instability test. This basic growth algorithm, due to Cieplak and Robbins,[10] leads to physically reasonable growth kinetics. For a complete catalogue of meniscus interactions, see Appendix 1.

4.3 Statistical Interpretation of Results

The most interesting feature of percolation theory is the existence of threshold values of critical parameters, below which the overall resistance of the network becomes infinite.[11,12] For example, below the *threshold pressure* P_c, the porous network will not be fully spanned by the invading phase. A *percolating cluster*, or continuous interconnected path linking the inlet to the outlet, will not be established. Further, above the threshold pressure P_c an infinite cluster of interconnected invaded pores exists (assuming an infinite lattice). Near the percolation threshold, the physical parameters of the system (e.g. correlation length, fraction of invaded pores) follow power laws of the type $(P - P_c)^{-x}$, thus they diverge as $P \rightarrow P_c$. These percolation statistical analyses can only be applied to non-wetting invasion (drainage), i.e. those dominated by applied pressure-generated "burst" interactions.

For IP models upon which this proposed work is based, statistical measures of the interface growth can be derived from the distribution of fingerwidths w, obtained by counting the number of adjacent invaded pores in discrete sections along all three

principal lattice directions and multiplying by the pore spacing d. In classical IP models a power law divergence of the form $w(\theta) \sim (\theta - \theta_c)^{-\nu}$ holds, where θ_c is the critical contact angle below which uniform pore filling occurs, leaving zero residual porosity, and ν ranges from 1.7-2.1, depending on the starting porosity.[10] In a similar fashion, the entrapped porosity should follow a similar scaling law with system size, i.e. $p(L) \sim (L - L_c)^{\nu}$, where p is a measure of the residual porosity and L is the lattice size. Fingerwidth counting and cluster counting algorithms are necessary to extract the fingerwidth distribution and residual pore size distribution from the data.

5 Construction of Computer Model

The mechanism for the computer model construction uses a cross-referencing data structures overlay. A full description of the pore status is required for the percolation statistics employed in the analysis of the output. See Appendix 2. The main Invasion Percolation algorithm is similar to that of Cieplak and Robbins (1990),[10] with the addition that periodic boundary conditions were employed. The algorithm for cluster counting, which enables the determination of percolation clusters and pore size distributions, as well as the simulation of enclosed loops (trapping), was similar to that of Hoshen and Kopelman (1976),[13] with provisions for periodic boundary conditions. The algorithm for fingerwidth counting was original to this work.

All computer code was written in the C and MATLAB programming languages. C code was used for the main program, including the finite difference routine for determining interface position. MATLAB executable files (MEX) were written to transfer data from C for graphics manipulation within MATLAB. All the simulations shown here were produced with a Digital Equipment Corporation (DEC) Alpha UNIX

workstation, which is equipped with a 500 MHz CPU and 1.0 GB of memory. For an example of the output used to troubleshoot the code in early stages of development, see Figure 4.

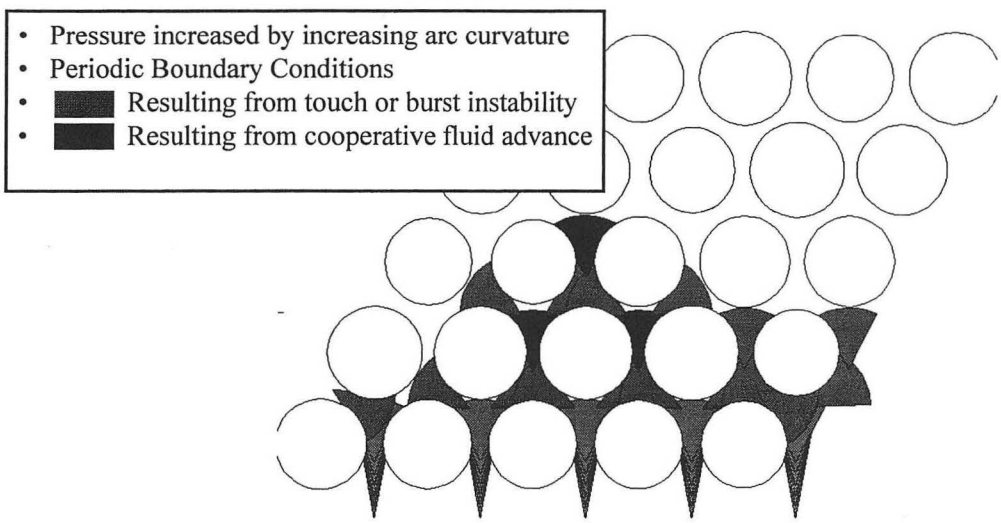

Figure 4 Example output to test interface growth algorithm, generated with a MATLAB 5.0 executable file.

6 Initial Simulation Results

6.1 Periodic Boundary Conditions

The small-scale simulations (40 x 40) of the basic invasion percolation simulation, with periodic boundary conditions, shown in Figures 5 and 6, demonstrate the basic mechanisms and effects that the model expects to reveal. At a constant contact angle of 45°, spontaneous wetting invasion occurs and cooperative pore filling mechanisms dominate. At long times, the system is spanned at the initial value of the curvature (simulated pressure) with no residual porosity.

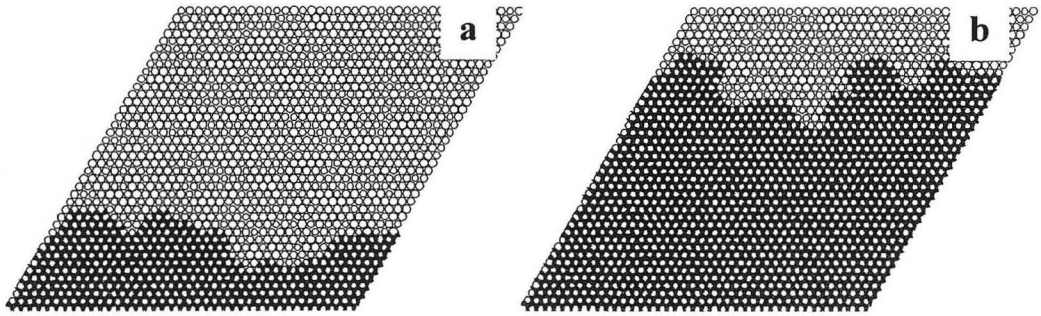

Figure 5 Invasion Percolation simulation, with periodic boundary conditions ($\theta = 45°$) illustrating cooperative fluid advance during spontaneous wetting invasion. Incipient uniform growth front, (a); and void free final microstructure, (b).

If the contact angle is increased to 60°, the pressure required to span the lattice is 2.3 times the pressure required at 45°. This corresponds to over-pressurized flow. The system becomes unstable against the formation of capillary fingers and residual porosity results in areas of non-uniform pore throat radii. Fewer cooperative pore filling mechanisms are operative ("overlaps" in Appendix 1) at the higher contact angle.

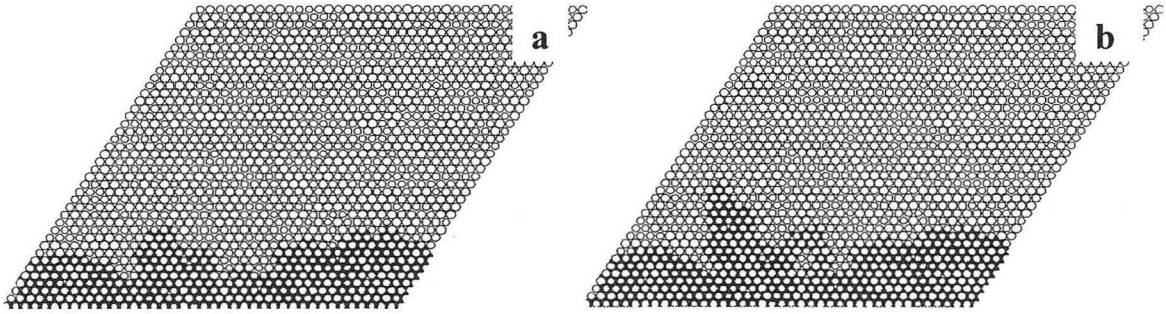

Figure 6 Invasion Percolation simulation at $\theta = 60°$, at an instability threshold where capillary fingering resulting from local heterogeneities in the pore space leads to residual porosity. Fewer cooperative fluid advance mechanisms are operative.

6.2 Divergence of Fingerwidth

To investigate these effects on larger scale systems the graphical output is reduced to a plot of the pore space, with each filled pore containing a single point. The pore space plots in Figure 7 are basic invasion percolation patterns from 100 x 100 lattices, with constant contact angles varying from 37 to 150 degrees. The process was initiated from the center of the lattice and the applied pressure incremented until the lattice was spanned. No periodic boundary conditions were employed. A plot of fingerwidth (normalized to the lattice constant) vs. contact angle is given in Fig. 8 to demonstrate the divergence of the fingerwidth. In these simulations the critical contact angle, below which complete pore filing is obtained, is 37°.

The results obtained in Fig. 8 are compared to those obtained by Cieplak and Robbins[10] to provide a check on the basic IP interface growth algorithm. The shape of the curve is explained by the type of interaction occurring at that range of contact angles. Between 41 and 37 degrees the plot diverges rapidly. In this range of contact angles cooperative fluid advance mechanisms control growth ("overlaps"). Between 41 and 56 degrees both overlaps and independent instabilities ("touches") are operative. Between 56 and 75 degrees both "touches" and "bursts" are operative (but not overlaps). Above 75 degrees burst instabilities alone are seen. The rapid divergence at $\theta < 37°$ agrees very closely with Cieplak and Robbins ($\sim 35°$). Another validation of the basic IP algorithm is the invariance of the fingerwidth in each principal lattice direction.

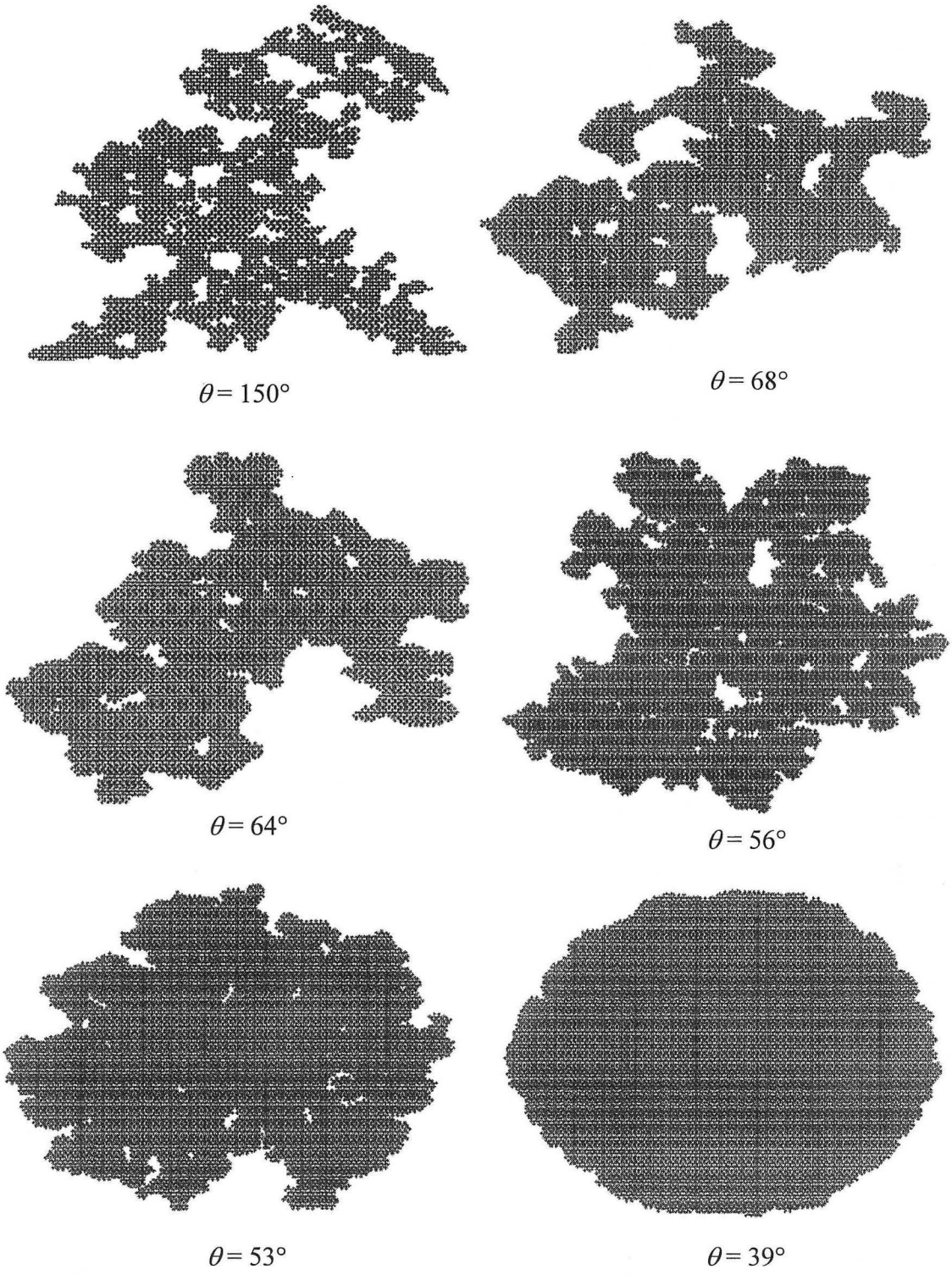

Figure 7 . Illustration of basic Invasion Percolation growth algorithm used in the model, on a 100 x 100 lattice with random pore size distribution, and initiated at the center of mass. Note the variation of porosity and fingerwidth with contact angle. Results for fingerwidth are given in Figures 8 and 9.

For the results to be statistically meaningful, the lattice size must be large enough for the fingerwidth distribution to converge. In addition, the starting ring must be of larger scale than the resultant fingerwidth in order to allow proper correlations (in the form of finger coalescence) in the initial stages of growth. To illustrate this, the fingerwidth results from 200 x 200 lattices with large starting rings are also given in Figure 8. The resultant curve appears more smooth than the 100 x 100 case.

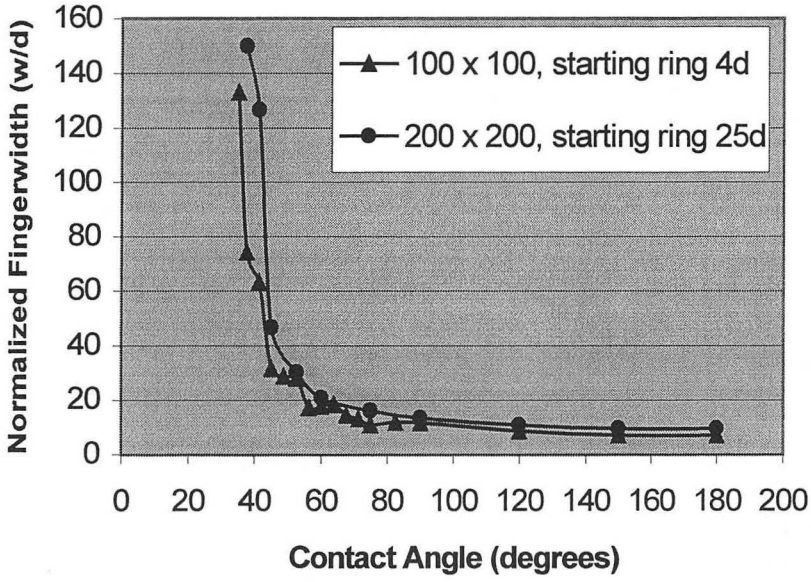

Figure 8 Plot of fingerwidth (normalized to the lattice constant d) vs. contact angle in Invasion Percolation simulation. The critical contact angle is 37°. Results are compared to those obtained by Cieplak, et al.[10] to provide a check on the basic IP growth algorithm.

7 Conclusion

A novel invasion percolation model is proposed to simulate the reactive melt infiltration of co-interpenetrating ceramic/metal composites. The invasion percolation growth algorithm upon which the model is based has been demonstrated on a 200 x 200 lattice, with fingerwidth divergence as was reported by Cieplak and Robbins in ref. 10. The assumption of quasi-static flow, essential for the application of pore-level models such as these, was demonstrated on a laboratory scale. Simulations like these, with the effects of surface reaction kinetics incorporated to simulate a high temperature process, will be demonstrated in exploring the trade-offs present in the processing of these systems. Infiltrated ceramic/metal composites must in general be processed in minimal time to prevent the formation of detrimental "core-shell" morphologies. This is most commonly done using an applied pressure at high temperature. This can lead to local instabilities and high growth rates of product phases in the pore space, which results in residual porosity and/or heterogeneous microstructures. The threshold values of critical parameters such as transformation rate, pressure, and system size determined in the computer simulations will reveal optimal combinations which lead to the most homogeneous, interconnected final microstructure, with the minimal interfacial reaction phase. At the same time a more fundamental understanding of the complex phenomena comprising this process is obtained.

[1] Broadbent, S.R., and Hammersley, J.M., *Proc. Camb. Phil. Soc.* **53** 629 (1957).
[2] Frisch, H.L., and Hammersley, J.M., *J. Soc. Indust. Math.* **11** 894 (1963).
[3] Lenormand, R. and Bories, S., *C.R. Acad. Sci. Ser. B* **291** 279 (1980).
[4] Wilkinson, D., and Willemsen, J.F., *J. Phys. A* **16** 3365 (1983).
[5] Chandler, R., Koplik, J., Leman, K., and Willemsen, J., *J. Fluid Mech.* **119** 249 (1982).
[6] Hubbert, M.K., "Darcy's Law and the Field Equations of the Flow of Underground Fluids," *AIME Petroleum Transactions* **207** 222-239 (1956).
[7] Koplik, J., Wilkinson, D., and Willemsen, J.F., "Percolation and Capillary Fluid Displacement," pp. 169-83 in *The Mathematics and Physics of Disordered Media*, Ed. Hughes, B.D. and Ninham, B.W., Springer Verlag, Berlin (1983).
[8] Washburn, E.W., *Phys. Rev.* **17** 374 (1921).
[9] Bird, R.B., Stewart, W.E., and Lightfoot, E.N., *Transport Phenomena*, Wiley, New York (1960).
[10] Cieplak, M., and Robbins, M.O., "Influence of contact angle on quasistatic fluid invasion of porous media," *Phys. Rev. B* **41** 16 11508-21 (1990).
[11] Stauffer, D. and Aharny, A., *Introduction to Percolation Theory*, Taylor & Francis, Bristol, PA (1991).
[12] Sahimi, M. *Applications of Percolation Theory*, Taylor & Francis, Bristol, PA (1994).
[13] Hoshen, J. and Kopelman, R., *Phys. Rev. B* **14** 3428 (1976).

Chapter Three Invasion Percolation Model with Reaction Kinetics

1 Introduction: Real Microstructures

One can further motivate a discussion of the modeling of composite fabrication using these methods by looking at real microstructures. The following micrographs demonstrate the processing regimes evident in these systems. In Figure 1a, from the work of Clement *et al.*[1], the *infiltration regime* is demonstrated as a low melting point wood's metal (Zn/Pb/Bi) alloy) has infiltrated a bed of crushed glass under pressure. No reaction occurs, and the metal does not wet the glass. The driving force for the process is the applied pressure alone. The cross-section, which was infiltrated from the bottom to the top, shows a rough interface, where capillary fingering dominates flow and residual porosity is evident. In contrast, the micrograph in Figure 1b, from the work of Xi *et al.*[2], which was infiltrated from the left to the right, depicts the *chemical reaction regime*, as Aluminum metal at 1500°C has infiltrated a reactive SiC/graphite preform. No external pressure was applied, the driving force is the so-called reactive wetting process, in which a chemical reaction leads to a surface wetting condition, which in turns leads to spreading on the surface. A "core-shell morphology" has resulted and the infiltration did not come to completion.

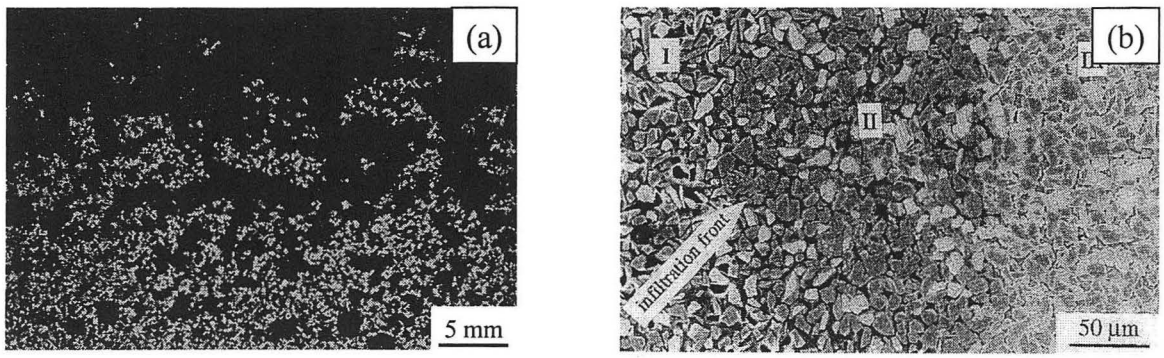

Figure 1 Woods metal infiltrating crushed glass (top to bottom) at 70°C, demonstrating infiltration regime, (a); and SiC/graphite preform infiltrated with Al metal at 1500°C, demonstrating chemical reaction regime, (b).

The novel Invasion Percolation model that was developed here accounts for both of these thermodynamic driving forces for infiltration, the applied pressure, and the surface reaction kinetics. In so doing it describes both capillary fingering effects and the development of core-shell morphologies. It enables the description of the time evolution of reaction byproduct phases, as well as the residual porosity. Statistics derived from percolation theory can be applied to determine the threshold values of the critical parameters pressure, transformation rate, and system size for the formation of a fully interconnected, void free microstructure with minimal interfacial reaction phase.

The following table illustrates the unique features of the model. Although Invasion Percolation and continuum models such as Darcy's Law both give estimates of average infiltration rate in non-reactive systems, only IP models describe pore level effects, such as capillary fingering, which can lead to residual porosity. Invasion Percolation models are concerned with over-pressurized flow only, but the novel IP model here includes both the applied pressure and the effects of the surface reaction

kinetics, which allows for the description of the time evolution of reaction byproduct phases.

	Average Infiltrn. rate	Capillary fingering	Surface reaction kinetics	Evolution of reaction phases
Novel IP	✓	✓	✓	✓
IP	✓	✓		
Continuum	✓			

Table 1 Illustration of the unique features of the model.

2 Interface Transformation Dynamics

2.1 Transformation Rate

Monte Carlo dynamics are embedded in the Invasion Percolation growth algorithm to incorporate the effects of the interfacial reaction on the system. The total transformation rate, R, can be expressed as

$$R = \sum_{i}^{n} 1/\tau_i \tag{1}$$

where n is the total number of sites on the active interface (and thus eligible to transform), and τ_i is the individual transformation time of each site. This total rate is related to the surface reaction rate constant

$$R \approx K = \exp\left(-\Delta G^{*}/kT\right) \tag{2}$$

where ΔG^{*} is the free energy of activation for the formation of the surface wetting condition. Thus the rate is proportional to the fraction of sites with the requisite free

energy to surmount the activation energy barrier, or alternatively, the probability of a particular site transforming at the temperature T. The transformation rate can be assigned based on empirical data of the evolution of the apparent contact angle with time. See Figure 2. As a first approximation such data can be fit to a simple plot of the form

$$\theta(t) = \theta_i + (\theta_f - \theta_i)\left[1 - e^{-Rt}\right] \tag{3}$$

Complex physical phenomena such as precursor film formation, surface oxide growth, surface alloying, and thin film growth contribute to the observed reduction in θ with time.

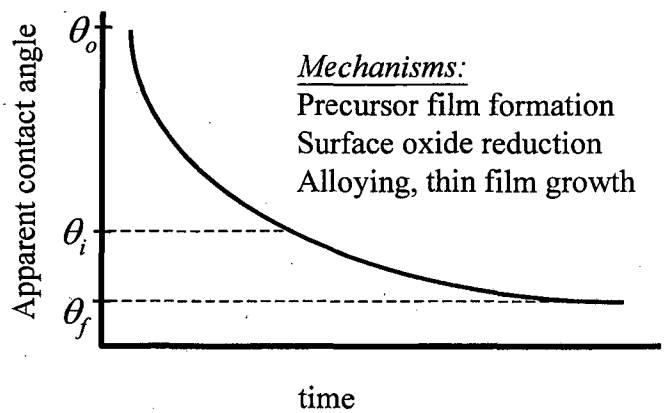

Figure 2 The transformation rate can be extracted from empirical data of the evolution of the apparent contact angle with time. The mechanisms of precursor film formation and oxide reduction occur uniformly as the vapor saturates the pore space. Alloying and thin film growth occur only when the interface is in direct contact with the lattice, and are modeled with equation (3).

Entirely deterministic arguments for modeling the transformation would require a completely characterizable distribution of activation energies on the lattice. In real materials the distribution of surface oxide thickness, surface activating agents, or other system-specific surface conditions that modify the wetting properties of the infiltrate are not sufficiently known, or would be mathematically intractable to apply. In addition, the processes governing the transformation to the wetting state are thermally activated, which

allows for a stochastic description. This postulate is fundamental to the classical rate theory of processes.

2.2 Transformation Time Intervals

Given the probabilistic nature of the transformation, it follows that the time intervals between successive transformation events on the interface are also determined probabilistically. The Poisson distribution describes the probability of events whose occurrences are statistically independent of one another. It is derived by realizing that the rate of change of the total number of events is proportional to the number of events occuring at any particular time.[3] A transformation process can be modeled stochastically as a Poisson process, provided the following conditions are met: 1) the forces governing the process remain constant (overall rate is constant), and 2) the probability of any site transforming is independent of the past development of the process, being dependent only on the total transformation rate.[4] Then time intervals must be chosen arbitrarily small enough so that only one transformation event occurs during the interval between times t and $t + \Delta t$. In the model presented here, after each transformation event the interface is allowed to equilibrate in the Invasion Percolation algorithm at the given pressure. The assumption of quasi-static flow allows for this process to be essentially instantaneous compared to the interval between transformation events.

From the zeroth term in the Poisson distribution, the cumulative distribution function for a Poisson process is given by

$$P(t) = 1 - e^{-Rt} \tag{4}$$

and represents the probability of a transformation event occurring between the time 0 and the time t. The individual time intervals between successive events in a Poisson process are exponentially distributed, and can be obtained by differentiating the cumulative distribution function with respect to t.

$$p(t)dt = Re^{-Rt}dt \tag{5}$$

Equation 5 gives the probability density function of individual transformation times on the lattice. Given that the cumulative distribution function is defined over the interval [0,1], one can generate uniformly distributed random numbers r_i and set $P(t) = r_i$. The individual transformation time intervals for a particular section of transforming lattice (random variates) can be sampled from the distribution in (5) by solving for the time t in (4).[5,6,7,8]

$$t_i = \left(-\frac{1}{R}\right)\ln(random[0,1]) \tag{6}$$

Each individual transformation time can be assigned by adding this interval to the current running process time during each Monte Carlo time step, which serves to establish a global clock for the system,

$$\tau_{trans} = t_i + \tau_{process}\,. \tag{7}$$

3 Product Phase Growth

3.1 Growth Rate Constant

An important feature of the model is that the rate, R, can be linked dynamically to the pore interstitial product phase growth that slows the infiltration rate. As demonstrated in Figure 3, at time t_g after the onset of the transformation event, the physical processes leading to the wetting condition on the lattice are essentially complete, and growth of the

product phase into the pore space begins. The thickness of the product layer formed can be input to the model from empirical data of product phase thickness vs. time, taken for the system of interest. As a first approximation the effect can be modeled using a simple parabolic growth rate constant

$$x^2 = kt \tag{8}$$

with x the thickness of the layer formed, t the time, and k the experimentally determined growth rate constant.[9] In this way the plugging of the pore space and the associated reduction in permeability to the fluid source can be simulated. This effect has been experimentally observed to cause "core-shell" morphologies that slow the infiltration.

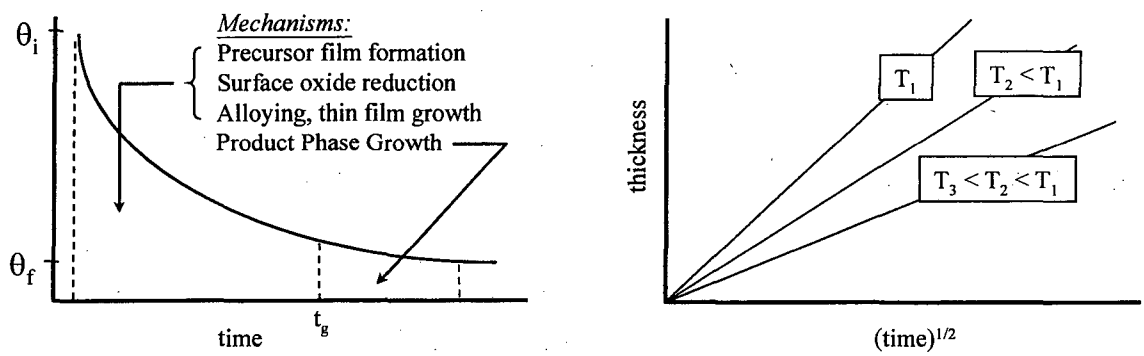

Figure 3 The interface transformation is linked with product phase growth using kinetic data taken for the system of interest. Higher transformation rates (implying higher temperatures) would normally be associated with higher growth rate constants.

3.2 Simulation of the Core-Shell Effect

The narrowing of pore throat openings has been experimentally observed to starve the interface for reactive metal. The effect is simulated in this model by computing the exact point at which an edge-spanning cluster of product phase forms. The transformation rate in that case serves as an upper limit for processes that form spanning

product phase clusters before the infiltration process comes to completion. The dynamics for product phase growth are implemented using the same basic methods used for the interface transformation. As the interface moves beyond each recently infiltrated section of the lattice, these sections are flagged and the kinetic growth rate constant applied. As the secondary phase grows on the surface of the lattice during each Monte Carlo time step, the lattice elements grow, beginning to consume and eventually completely filling the pores. An algorithm is called to determine the time at which an interconnected path of pores filled with secondary phase first forms. High volume fractions of secondary phases can be detrimental to both the mechanical and thermal properties of these materials. A basic flowchart of the computer model is given in Appendix Three.

4 Initial Simulation Results

To illustrate the Invasion Percolation simulation with chemical reaction kinetics, using the same model system as shown in Figure 2-5, (spontaneous wetting invasion, no chemical reaction), the initial contact angle was set to 75° (non-wetting). See Figure 4. To simulate the effect of reactive infiltration, the interface was allowed to transform to a wetting condition, with individual transformation times randomly sampled from the exponential distribution in equation (5). In this example, the transformation rate is instantaneous (very large rate R) once initiated to simplify the discussion. In later simulations the transformation is allowed to occur continuously, which requires a longer time to achieve the wetting transition and produces more realistic transformations. After each transformation event, the interface equilibrates according to the Invasion Percolation growth algorithm. Referring to Figure 4, the transformation times indicated, τ, are found

by randomly sampling the exponential waiting time distribution function using a pseudo-random number generator. The lattice site with the lowest transformation time, τ_l, achieved the wetting transition first. The subsequent quasi-static advance of the interface in the pore space adjacent to this site is illustrated.

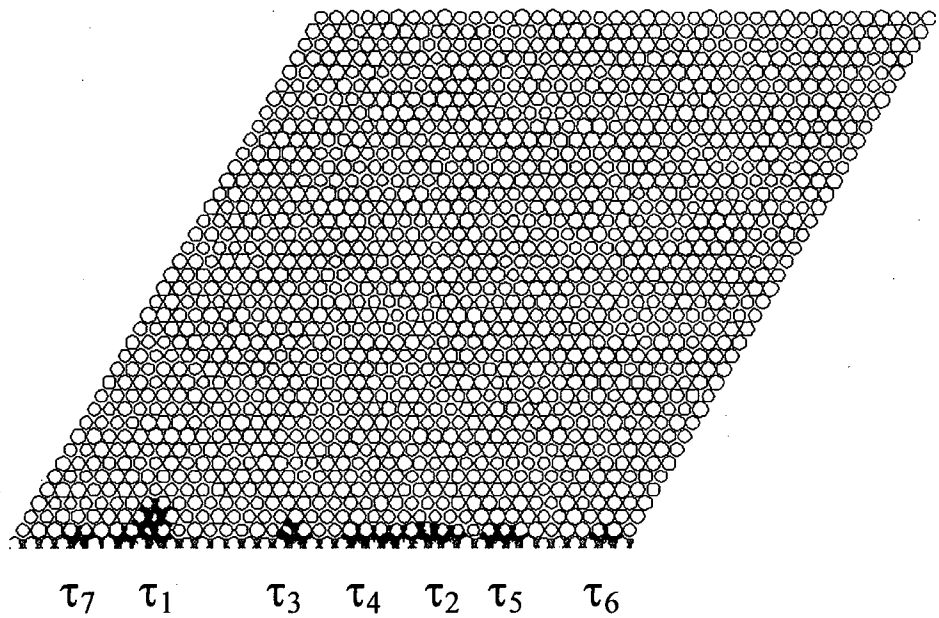

Figure 4 Illustration of the interface transformation at low pressure. At equilibrium, the individual transformation intervals are randomly sampled from the exponential distribution ($\tau_1 < \tau_2 < \ldots \tau_7$).

4.1 Chemical Reaction Regime

Chemical reaction regime is observed at low applied pressure (simulated with large radius of curvature) and high transformation rate. The principal driving force is the liquid spreading, or reactive wetting process, that accompanies the transformation. In Figure 5, time step snapshots of the simulation are shown, at short and long times. A uniform interface growth front has developed, with no residual porosity. A core-shell

morphology would result under these conditions if the infiltration does not come to completion before the pore space fills with reaction byproduct phases.

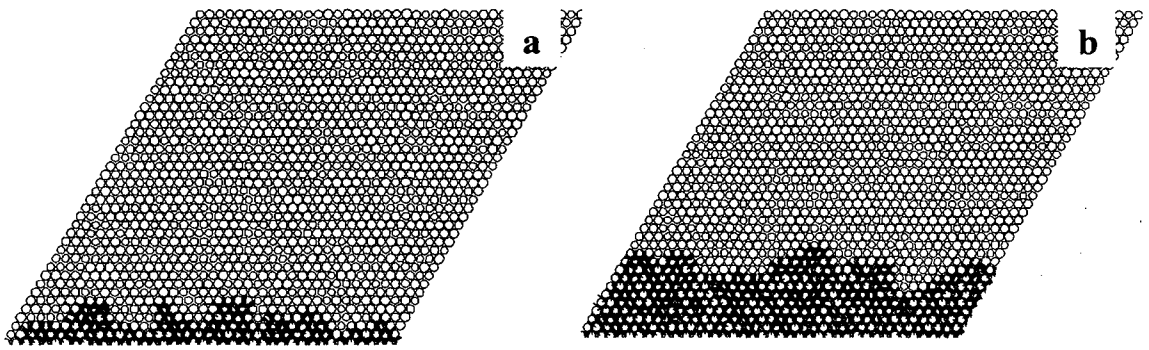

Figure 5 Time step snapshots of the IP Simulation at low pressure, high transformation rate, demonstrating chemical reaction regime. At short times small infiltration islands form, (a). At long times the interface advances uniformly, with a high occurrence of cooperative pore filling mechanisms, (b).

4.2 Infiltration Regime

The infiltration regime is observed at higher applied pressure (simulated with smaller radius of curvature) and low transformation rate. The principal driving force is the applied pressure. For example, if the external pressure in the simulation shown in Figure 5 is doubled, an effect similar to the one described in basic Invasion Percolation (Fig. 2-6) is seen. After each transformation event the interface equilibrates quasi-statically at the higher pressure. In Figure 6 a rougher interface is observed, with an increased penetration distance in local areas of small pore throat radii. As the system evolves, developing capillary fingers will intersect areas of non-adjacent interface, causing pore space trapping to occur. These regions are undesirable if they lead to enclosed porosity or areas of completely reacted interfacial phases.

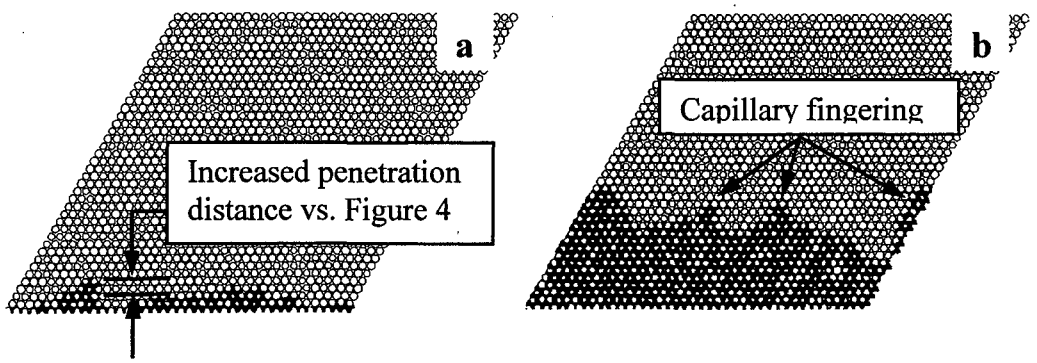

Figure 6 Time step snapshots of the IP Simulation at higher pressure, low transformation rate, demonstrating infiltration regime. At short times the interface penetrates to increased distances in local areas of small pore throat radius, (a). At long times capillary fingers form that may intersect and lead to pore space trapping and residual porosity, (b).

5. Quantification of Results

5.1 Divergence of the Fingerwidth

The results of the basic Invasion Percolation simulations were reported in Chapter Two in terms of the divergence of the fingerwidth. Such plots could be compared with previous work to validate the accuracy of the Invasion Percolation growth algorithm. Using statistics derived from percolation theory, threshold values of critical parameters that lead to the desired microstructure can be found. Such scaling laws would have the form

$$W(P) = (P - P_c)^{-\gamma} \tag{9}$$

where W is an output parameter such as fingerwidth, P is the applied pressure at constant transformation rate and initial porosity, and γ is the experimentally determined scaling exponent. Alternatively, W could scale with transformation rate, at constant pressure and initial porosity. The threshold value is defined as the value of the pressure or transformation rate at which the fingerwidth diverges and complete pore filling occurs.

Another interesting scaling law to investigate is the how the residual porosity scales with system size;

$$\phi(L) = (L - L_c)^{\beta} \tag{10}$$

where ϕ is some measure of the residual porosity after infiltration, L the system size, and β the scaling exponent. In investigating the physics of equations (9) and (10) the theory of finite sized scaling can be useful. These scaling laws can be used to relate the simulation results of finite size systems to the behavior of macroscopic systems. For a discussion of the method, the reader is referred to Stauffer *et al.*[10] The study of the finite size effects in materials processing is a new field of interest in materials science that can yield new insight on the mesocopic scale, and in relating the microscopic properties of a system to its macroscopic behavior. Such numerical investigations typically are quite computationally extensive, however, requiring large amounts of CPU time. For the purposes of this work, it was deemed more advantageous to describe the results in terms that are most familiar to the experimental materials scientist. In addition, some correlation between microstructure and mechanical properties was sought. The two methods discussed below involve the use of process maps to delineate acceptable processing regimes, and the determination of the residual pore size distribution and its link to the statistical probability of fracture.

5.2 Process Mapping

The computer simulations are designed to determine the optimal combinations of transformation rate, applied pressure, and initial porosity that lead to the most desirable final microstructure. These conditions can be laid out on a process map, with axes the

applied pressure and the transformation rate, with the residual porosity or fingerwidth laid out as contours as in a topographic map. The limits of the process, determined as the points at which the core-shell effect is detected at the given rate and pressure, and the points at which the capillary length criterion is violated, can be delineated as phase boundaries on the map.

5.3 Residual Pore Size Distribution and Mechanical Properties

The final microstructure can be linked to the mechanical properties (in particular the probability of fracture) through an analysis of the residual pore size distribution. Using a simple Griffith criterion for fracture, the critical flaw size for a given applied stress can be predicted if the fracture toughness of the material is known. Through the following analysis of the residual pore size distribution, one can obtain the probability that the largest flaw in a population of flaws is smaller than the critical flaw size for fracture.

5.3.1 Determination of Residual Pore Size Distribution

The raw data obtained from the pore cluster counting algorithm is binned to minimize the root mean-square deviation of the errorbars covering multiple simulations. This is done by adjusting the binwidth while producing histograms of the residual pore areas. The probability that a pore belongs to a particular bin is

$$p_i = \frac{n_i}{\sum_i n_i} \tag{11}$$

where n_i is the number of pores in a bin of width w_i. This probability is equal to the probability of a pore being of exactly size x_i, the bin location, multiplied by the binwidth,

$$p_i = p(x_i)w \cdot \tag{12}$$

As the number of bins tends to infinity, this discrete distribution tends to the continuous probability distribution function, *P(a)da*, which gives the probability that a randomly sampled pore has area between *a* and *a* + *da*,

$$\int P(a)da = \lim_{i\to\infty}\sum_i \frac{p_i}{w} = \lim_{i\to\infty}\sum_i p(x_i) \cdot \tag{13}$$

Graphically, the pore size distribution function is obtained by plotting the individual bin probabilities, divided by the binwidth, versus the bin location (p_i/w vs. x_i).

5.3.2 Pore Cluster Probability

It is necessary to obtain the pore cluster probabilities to determine the probability of failure based on pore cluster size. Pore cluster probability is defined as the probability that, randomly sampled from the distribution of residual pore sizes, a given pore belongs in a cluster of *n* connected pore sites. The procedure is as follows.

The normal (Gaussian) distribution is expected to closely represent results in which simulated statistics are generated with uniformly distributed random numbers. A Gaussian curve fit to the residual pore size distribution function is obtained by minimizing the chi-square statistic. If the probability distribution function is resolvable to *n* main peaks, representing the residual pore cluster sizes, and the observed data is contained in *k* bins, this statistic can be represented as[11]

$$\chi^2 = \sum_{i=1}^{k} \frac{(P_i(a) - g_i(a))^2}{g_i(a)} \tag{14}$$

with P_i the value of the observed distribution function in the i-th bin, and g_i representing the expected value in this bin according to the curve-fit Gaussian function, which includes the sum of the individual Gaussians corresponding to each pore cluster size n,

$$g(a) = \{g_1(a) + g_2(a) + g_3(a) + \ldots g_n(a)\}. \tag{15}$$

The areas under the Gaussian curves enable a relationship between the discrete probability distribution function $\underline{P}(a)$ and the continuous $P(a)$. The discrete probabilities $\underline{P}_n(a)$ are defined as the probability that a given pore, *relative to the total number of pores*, belongs to a cluster of n pores.

$$\underline{P}_n = \frac{\int g_n(a)da}{\sum_{j=1}^{\infty} \int g_j(a)da} \tag{16}$$

The mean cluster size is related to the discrete probability distribution. This relationship

$$\bar{a} = \int_0^{\infty} aP(a)da = \sum_{n=1}^{\infty} \mu_n \underline{P}_n \tag{17}$$

where $\bar{a}$ is the total mean pore size, and μ_n is the mean pore cluster area for each discrete pore cluster, is essential when the discrete probability distribution function is not resolvable for every pore cluster size, which is usually the case for small systems. The discrete pore probability distribution, for pore clusters larger than can be accurately resolved from the probability distribution, is simply

$$\sum_{n=m+1}^{\infty} \mu_n \underline{P}_n = \bar{a} - \sum_{n=1}^{m} \mu_n \underline{P}_n \tag{18}$$

Rearrangement of equation (18) leads to the discrete pore cluster probability, Π, which is the statistically weighted probability, *relative to the total pore area*, that a randomly

sampled pore belongs to a cluster of size n. For example, the probability that a randomly sampled pore is of a cluster greater than an m-cluster, is given by

$$\Pi_{n>m} = 1 - \frac{1}{\bar{a}} \sum_{n=1}^{m} \mu_n \underline{P}_n \cdot \tag{19}$$

Similarly,

$$\Pi_n = \frac{1}{\bar{a}} \mu_n \underline{P}_n \cdot \tag{20}$$

5.3.3 Mechanical Properties

The weakest link statistical theory of brittle fracture, due to Weibull,[12,13] can be derived from the pre-existing flaw size distribution $q(a)$, where a is the equivalent length of the Griffith flaw normal to the maximum principal stress.[14] For a complete development of the argument, see Appendix Four. The probability of failure P_c in a unit volume V at an applied stress σ_{app} is given by

$$P_c(\sigma_{app}) = 1 - \exp\left(-V \int_{a_c}^{\infty} q(a) da \right) \cdot \tag{21}$$

Here the critical flaw size a_c would be a function of the defect position in the stressed body with respect to the applied stress, and the defect aspect ratio, which could lead to higher stress concentrations at the crack tip. From a simple Griffith-type analysis, assuming type I loading conditions (tensile stresses only) and an elliptical-shaped crack, $a_c \sim (1/2\pi)(K_{IC}/\sigma_F)^2$.

Thus, with a known value of the fracture toughness, the failure probability for a given microstructure is easily obtained, provided the residual pore size distribution

function is known. It is clear that equation (19) is a discretized version of the following continuous relationship

$$\Pi_{a>a_c} = 1 - \frac{1}{\bar{a}} \int_0^{a_c} aP(a)da \cdot \tag{22}$$

Since the probability *P(a)* is expressed relative to residual porosity, normalizing to the total system area is necessary. Then this normalized probability can be discretized and directly substituted into the integrand for the exponential in equation (21) in order to determine failure probability over any assumed total volume (or area) of the material. For simplicity a unit volume of material will be assumed for the Weibull statistics applied in this work.

6 Experimental Plan

The aluminum/Silicon Carbide system was used as a model system for the infiltration simulations, because a large volume of wetting data is available. The model can be applied to any system, provided empirical data of the contact angle evolution, correlated with chemical composition on the surface, is available. Kinetic data of product phase growth with temperature is required to input the growth rate constant and study the core-shell effect. The following systems are to be studied, at values of applied pressure set to simulate feasible processing conditions, ranging from 1 to 10 psig.

6.1 Model Systems

1. *Zero transformation rate, zero kinetic growth rate constant* studies are designed to be a baseline for all subsequent simulations. Multiple seedings of the random number

generator are to be used to evaluate the precision and convergence of the results. These simulations occur within the narrow range of the applied pressure between total infiltration and the formation of the percolation cluster at the critical value p_c.

2. *High transformation rate, very low kinetic growth rate constant* studies are designed to simulate a high temperature process, possibly with surface active wetting agents that accelerate wetting kinetics, and with alloying element additions that suppress the formation of secondary phases. An example is the infiltration of a carbon-rich SiC porous body by an Al-20Si alloy, in which the Silicon in the alloy suppresses the growth of Al_4C_3 on the surface.
3. *High transformation rate, finite kinetic growth rate constant* studies are designed to simulate a high temperature process, in systems where the growth of secondary phases is a function of temperature.
4. *Low transformation rate, low kinetic growth rate constant* studies are designed to simulate a low temperature process where no reaction occurs, or a non-wetting surface condition. These systems should take long times to completion, and the primary driving force is an applied pressure.
5. *Intermediate transformation rate, finite kinetic growth rate constant* studies are designed to delineate the points on the process map where the core-shell microstructure is first observed.

6.2 Incompressible Phase Assumption

All the model systems discussed above can be simulated with or without using an invasion percolation trapping mechanism. When the displaced secondary phase is liquid,

as is the case in invasion percolation modeling of oil reservoirs, it is reasonable to assume that the formation of incompressible loops leaves areas in the pore space that are not invaded. When the displaced phase is a gas such as argon or nitrogen, as is expected in a composite fabrication process, diffusion of the gas out of the entrapped areas would be required to relieve the back-pressure in the enclosed sections of the pore space. In this case gas bubbles would act as local barriers to infiltration. In the simulations studied in this work the diffusion out of the pore space of inert gases is not accounted for, and thus is assumed negligible. If the backside of the sample is evacuated, however, and a pressure applied to the front side, as could also be envisioned for these materials, no invasion percolation trapping mechanism would be required. Nevertheless, the optimum microstructures obtained in the simulations with the trapping mechanism active would be best case, because they would be produced by filling the pore space with infiltrate, and would not involve closing porosity with the formation of a secondary phase. Thus it should be useful to compare results to simulations when the trapping mechanism is activated.

7 Random Numbers in Simulation

The generation of random numbers is an essential feature of Monte Carlo simulation techniques.[15] In deterministic models, neither the dependent or independent variables are permitted to be random, so exact numerical or analytical solutions exist. The characteristics governing the system are known empirical relationships. In stochastic models, at least one of the system characteristics is governed by a probability distribution function. In this model the lattice disk radii and interface transformation times are the

random variables. A random variable is a real valued function defined over a sample space associated with the outcome of a conceptual chance experiment.[5] The discrete individual values that are randomly sampled from this probability distribution function are termed the random variates. Simulation statistics are obtained by supplying pseudo-random numbers into the system, where the system is represented by a probabilistic model, and obtaining random variates (numbers) as answers. Thus one replaces an actual statistical universe of elements by its theoretical counterpart. These probability distribution functions are the closest approximation that can be made to the actual mathematical description, which is unattainable due to the complexity of the system. Several simulations run under the same conditions, each started using a different seed of the pseudo-random number generator, must be run in order to obtain sufficient precision in the results.

[1] Clement, E., Baudet, C, Guyon, E., and Hulin, J.P., "Invasion front structure in a 3D model porous medium under a hydrostatic pressure gradient", *J. Phys. D.*, **20** 608-15 (1987).
[2] Xi, X.M., and Yang, X.F., "Spontaneous Infiltration of Aluminum-Silicon Alloy into Silicon Carbide Preforms in Air", *J. Am. Ceram. Soc.*, **79** [1] 102-108 (1996).
[3] Boas, M.L., in *Mathematical Methods in the Physical Sciences*, Wiley, New York (1983) p. 728.
[4] Feller, W., in *Introduction to Probability Theory and its Applications*, Vol. 1, 2nd Ed., John Wiley and Sons, New York (1957), pp. 146-63, 444-61.
[5] Naylor, T.H., Balintfy, J.L., Burdick, D.S., and Chu, K., *Computer Simulation Techniques*, John Wiley and Sons, New York (1966), pp. 1-122.
[6] Kleijnen, J.P.C., *Statistical Techniques in Simulation*, Marcel Dekker, Inc., New York (1974), pp. 1-60.
[7] Binder, K., *Monte Carlo Methods in Statistical Physics, 2nd. ed.*, Ed. K. Binder, Springer-Verlag, Berlin (1986), pp. 1-45
[8] Maksym, P.A., "Fast Monte Carlo simulation of MBE growth," *Semicond. Sci. Technol.* **3** 594-96 (1988).
[9] Chidambaram, P.R., Edwards, G.R., and Olson, D.L., "Kinetics of Interlayer Formation on Polycrystalline α-Al_2O_3/Copper-Titanium Alloy Interface", *Metallurgical and Materials Transactions A*, **25A** 2083-2090 (1994).
[10] Stauffer, D. and Aharny, A., *Introduction to Percolation Theory*, Taylor & Francis, Bristol, PA (1991).
[11] Press, W.H., Teukolsky, S.A., Vetterling, W.T., Flannery, B.P., *Numerical Recipes in C*, Cambridge University Press, Cambridge, UK, (1992)
[12] Weibull, W., *Proc. Ing. Vetenskapskad.*, 151 (1939).
[13] Weibull, W., *J. App. Mech.*, **18** 293 (1951).
[14] Hunt, R.A., and McCartney, L.N., "A new approach to Weibull's statistical theory of brittle fracture", *Int. J. Fracture*, **15** 4 365-75 (1979).
[15] Hammersley, J.M., and Handscomb, D.C., *Monte Carlo Methods*, Methuen and Co., London (1964).

Chapter Four Baseline Simulation

1 Lattice Initial Conditions

A study was completed without simulating a transformation, encompassing the narrow pressure range between the formation of a percolation cluster and total infiltration, to establish the methodology. The pressure ranged from the percolation threshold pressure for the formation of a single percolating pore just spanning the entire system, P_c, to a pressure above P_c when divergence of the fingerwidth (complete pore filling) was first observed. The contact angle was set at 60°, initially non-wetting, but close to the wetting transition for the lattice under investigation. This value was also found to be viable when simulating reaction/infiltration, which is discussed later. A lattice of size 233 x 233 was chosen, with a lattice site spacing of 50 μm, corresponding to a system size of 1 cm with lattice grain radii randomly distributed between 18-24 μm. This produced a random pore size distribution between approximately 150 and 500 μm^2 area, or equivalently half-penny shaped flaws with radii ranging from 7.5 to 12.8 μm. The narrowest pore throat opening ranged from 2 to 12 μm, taken as the lattice disk closest approach position. The total overall porosity, determined by fractional area, was found to be 0.327. This lattice, termed *Lattice I*, was found to produce all the featured interactions of the invasion percolation growth algorithm, and was also found to be reasonable when compared to the composite materials produced experimentally by the methods described in Section 3 of Chapter 2.

The size of the pore throat opening determines the pressure required for the penetration of a particular pore. With a mean "hydraulic radius" determined from the specifications for *Lattice I*, a pressure range for the baseline simulation was established at

0.268-0.281 ATM (2.68×10^{-5} dynes/cm^2 – 2.81×10^{-5} dynes/cm^2), or approximately 3.94 – 4.14 psi. The surface tension of the invading fluid was taken to be 375 dynes/cm, which was measured on an Aluminum alloy containing 9 percent Magnesium and 13 percent Silicon at a temperature of 1050∘C.[1] This alloy was found to be favorable during wetting kinetic studies on SiC because the Si suppressed the formation of Al_4C_3 on the surface, and when processed in a nitrogen atmosphere the Mg contributed significantly to the reduction in alloy surface tension, which assists liquid spreading.

2 Microstructure

The two critical pressures, one a percolation threshold pressure for the formation of a single system spanning pore cluster (at 0.267 ATM), the other a critical pressure for the divergence of the fingerwidth (at 0.281 ATM), produced typical microstructures as shown in Figures 1a and 1b. This narrow range of pressure producing large changes in structure is typical of percolative systems near a critical point.

The raw data for the sum of 8 simulations, each with a different random number seed, is plotted in Figure 1c. Near the critical pressure for divergence of the fingerwidth, the probability of occurrence of a pore of discrete size one approaches unity. This is expected as the first and only pore to appear as the fingerwidth diverges would be of cluster size one. At lower pressures, the plot spreads out as cluster sizes greater than one appear. Near the percolation threshold, the plot is most spread out as larger pore clusters dominate.

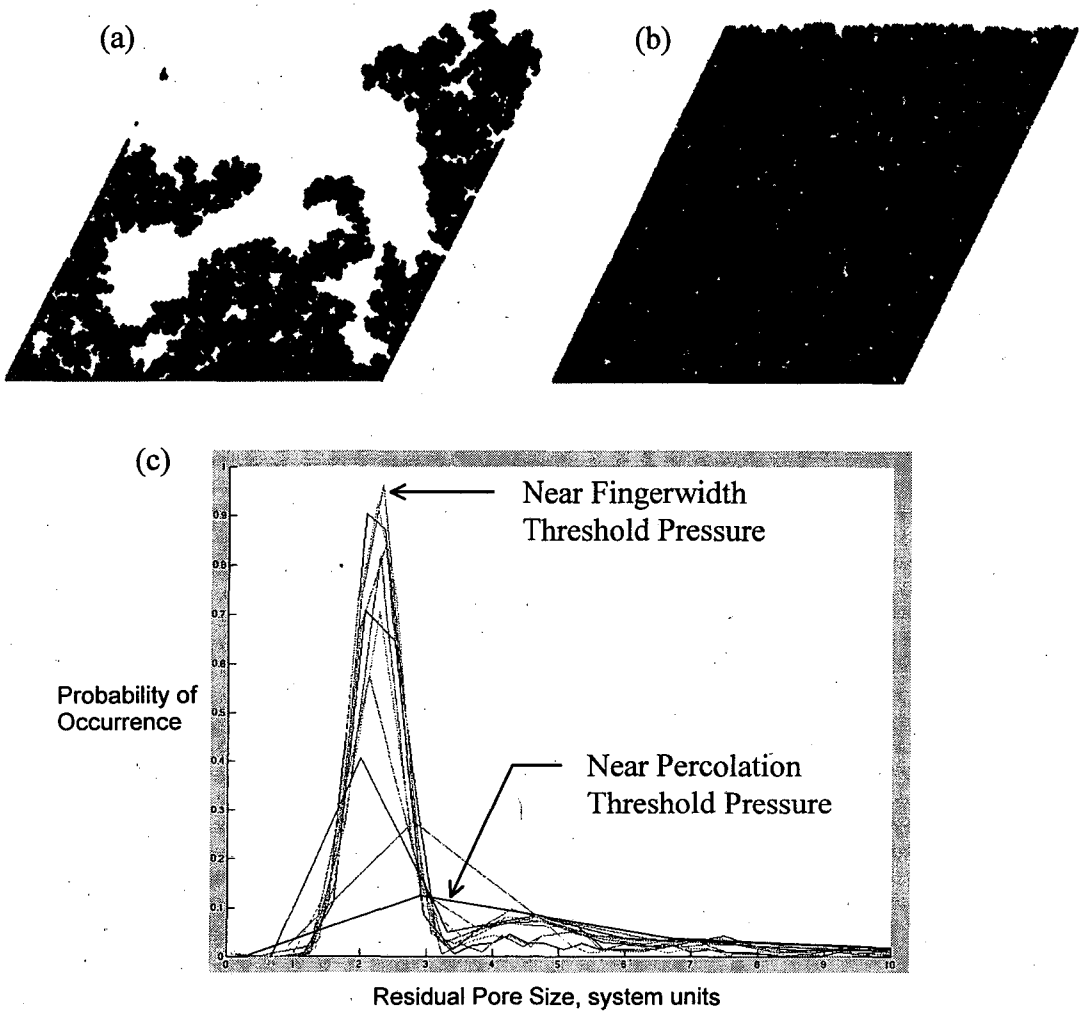

Figure 1 Residual porosity for the baseline simulation; (a) approaching the threshold pressure for percolation; (b) approaching the critical pressure for divergence of the fingerwidth; and (c) associated probability distribution functions spanning the entire pressure range.

3 Data Reduction

The raw data for all pressures, as shown in Figure 1c, were binned at identical binwidths and bin locations. Optimally, the minimum of the root mean square deviation of the errorbars over the entire simulation set is sought. For example, Figure 2 shows the data for one set of simulations taken at the same applied pressure but 8 different random

number seedings. After the optimal values of binwidth and bin location are found, the curves are fit to Gaussian approximations and the pore cluster probabilities obtained.

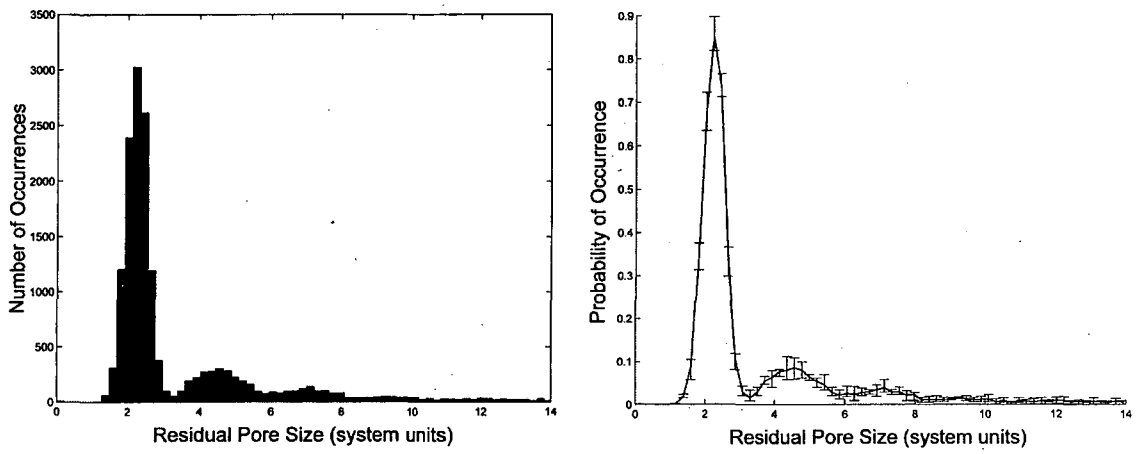

Figure 2 The histogram and errorbar function of the baseline simulation, at applied pressure 0.272 ATM. The binwidth and bin locations are determined by minimizing the root mean square deviation of the errorbar function over the entire simulation set.

The Gaussian curve fit obtained for the simulation at 0.272 ATM is shown in Figure 3. The chi-squared statistic for this simulation was 0.003, indicating a good fit to the data using the normal (Gaussian) distribution. The peaks at cluster sizes 4 and above are not readily resolvable and not amenable to an accurate curve fit procedure. Using the method outlined in Chapter 3, the probability of occurrence of these larger pore clusters is readily attainable, given the well defined peaks corresponding to the smaller pore clusters. Pore cluster probability plots, which are normalized to account for the size of the individual pore in the larger clusters, were found to be effective ways to statistically represent the change in microstructure resulting at different values of the applied pressure.

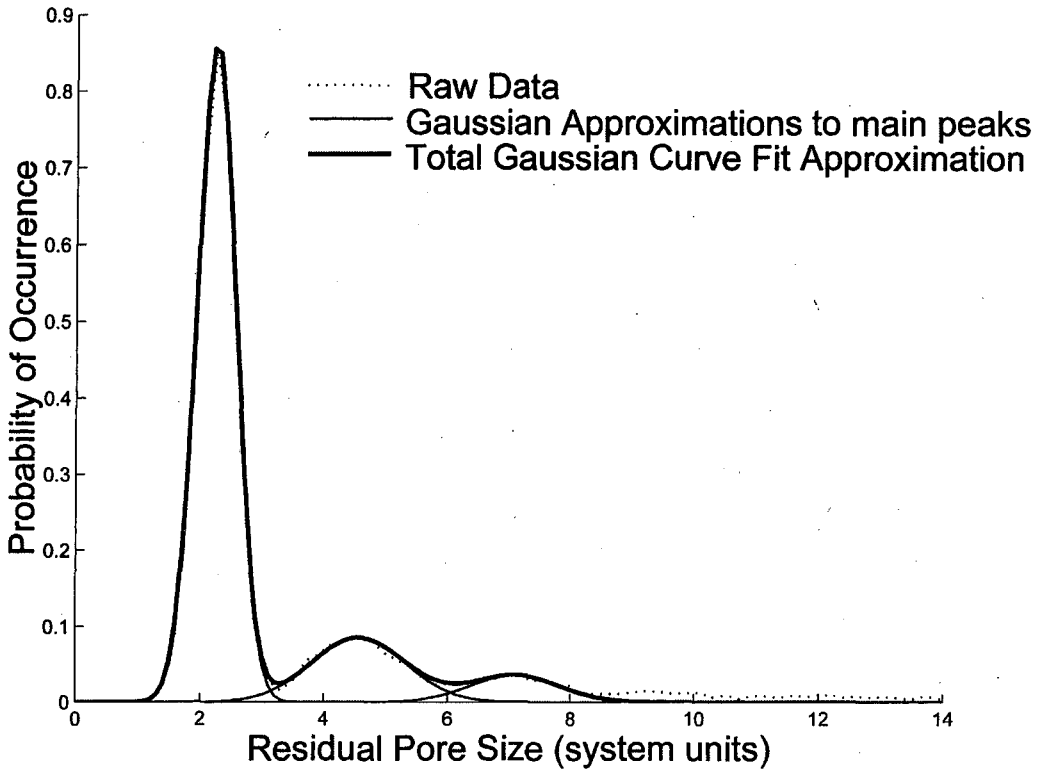

Figure 3 Gaussian curve fit to the baseline simulation (0.272 ATM). The individual peaks at pore cluster sizes 4 and greater are not accurately resolvable using these methods.

4 Pore Cluster Probability and Weibull Survival Probability

Figure 4 is a plot of the pore cluster probabilities for the baseline simulation. Pore cluster probability was defined in Chapter 3 as the statistically weighted probability that a randomly sampled pore in the microstructure belongs to a cluster of n pores. Normalizing for actual porosity allows for the application of Weibull statistics for the determination of failure probability from residual pore size distribution. The method,

outlined in Chapter 3-5, involves integrating the residual porosity over the entire sample volume (or area).

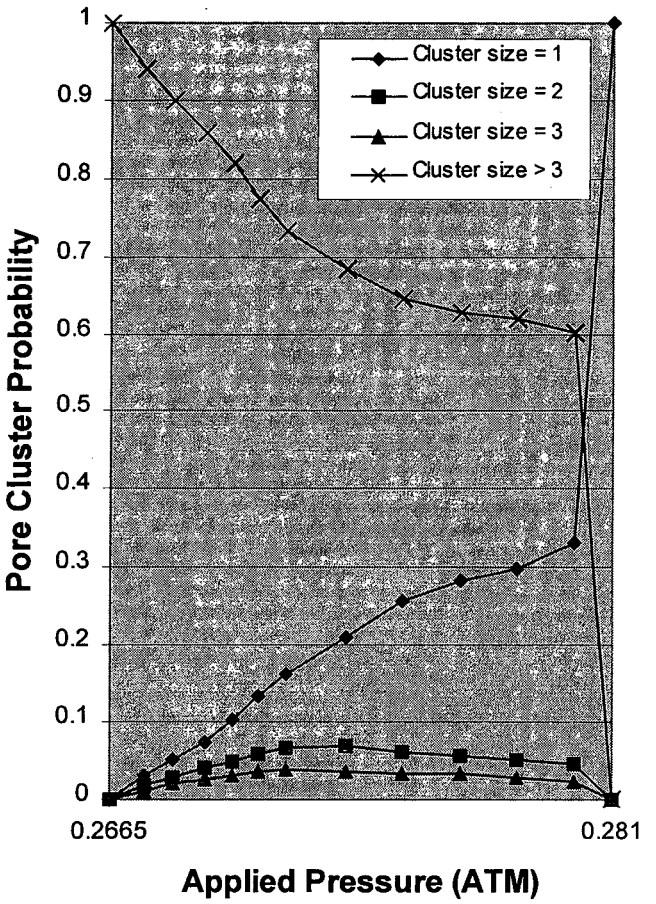

Figure 4 Plot of pore cluster probability for the baseline simulation. The applied pressure ranges from the threshold pressure for percolation (0.267 ATM) to the critical pressure for the divergence of the fingerwidth (0.281 ATM).

It is interesting to note the wide variety of microstructures that resulted in the baseline simulation over a small range of applied pressure. This is primarily a geometric effect due to the proximity of the surface contact angle (60°) to the honeycomb lattice angle of *Lattice I.* It was found experimentally that angles in this range will produce simulations that reveal critical point phenomena. Thus, by design a relatively small change in pressure produced simulations to investigate both the initial entry pressure of

the lattice, and the critical pressure for complete infiltration. If the contact angle is increased from 60°, the range over which these extremes are observed would also increase. This becomes important when the surface reaction is incorporated in the process.

The Weibull failure probability plots for the baseline simulation are shown in Figure 5. A fracture toughness of 9.4 $MPam^{1/2}$ was assumed, a value measured for an Al/SiC composite fabricated by Hannon *et al.*[3], and the failure probability plotted as a function of applied stress. The critical flaw size for the applied stress was determined assuming mode I loading and an embedded elliptical flaw with aspect ratio 3, using the method given by Anderson.[4] The number of critical flaws found in the unit volume of material was directly substituted into equation 3-21 to determine failure probability.

$$P_c(\sigma_{app}) = 1 - \exp\left(-V\int_{a_c}^{\infty} q(a)da\right) \tag{1}$$

This method accounts for the fact that at a given value of the applied stress the critical flaw a_c could be smaller than the largest flaw produced in the microstructure. Thus there is a population of potential critical flaws. This is essential since the residual porosity must be integrated over the entire microstructure when searching for a critical flaw. Since the number of critical flaws per unit volume is a function of the applied stress, equation (1) is commonly integrated over the volume to give,

$$P_c(\sigma) = 1 - \exp\left(-\sigma/\sigma_0\right)^m \tag{2}$$

where σ_0 is a normalizing parameter and m is the Weibull modulus, or shape factor, which is proportional to material homogeneity and is a broad indication of a material's mechanical reliability. Equation (2) may be rewritten as

$$m\ln(\sigma) = \ln\ln\left(\frac{1}{P_s}\right) + \ln(\sigma_0) \tag{3}$$

where P_s is the probability of survival ($P_s = 1\text{-}P_c$). Equation (3) is used to generate Weibull failure probability plots as demonstrated in Figure 5.

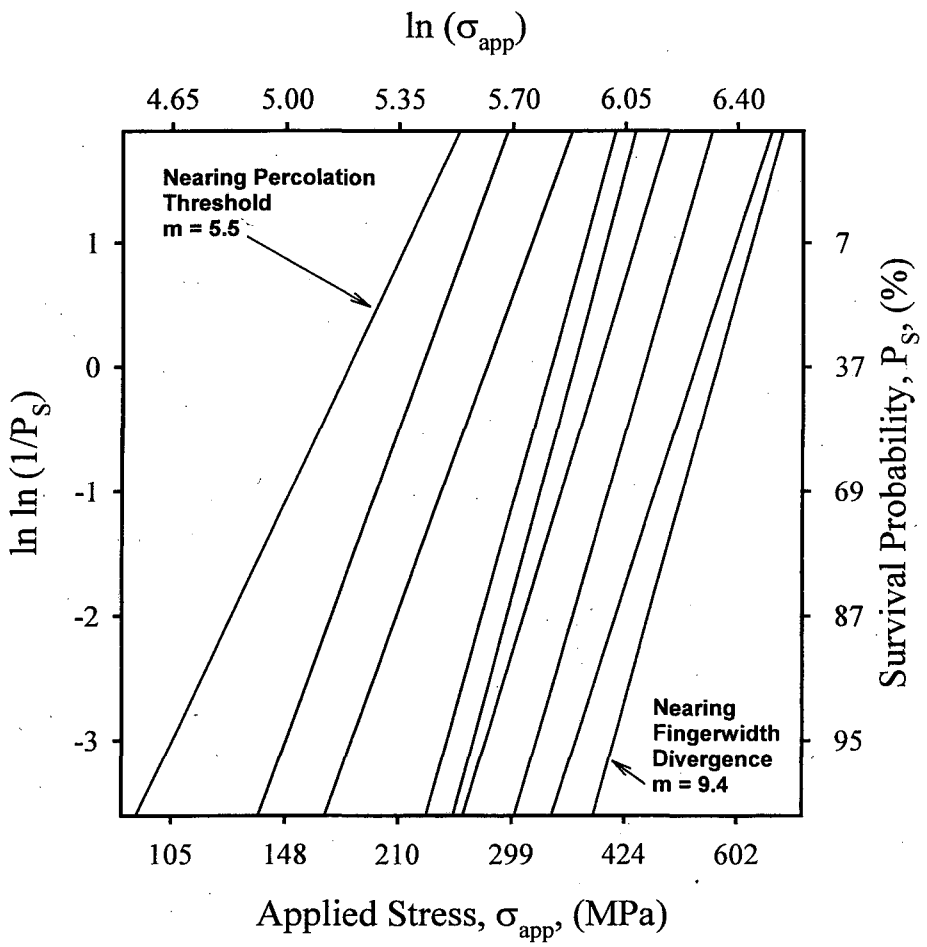

Figure 5 Weibull survival probability plot for the baseline simulation, with pressures ranging from near the percolation threshold pressure to near the critical pressure for the divergence of the fingerwidth.

The combination of pore cluster probability plots and Weibull survival probability plots enables a comparison of the microstructural changes occurring within one simulated material group, and correlation with the expected mechanical properties. In the baseline simulation shown here, as the pressure increases from the initial percolation threshold pressure (lowest pressure which leads to a system spanning cluster) to the critical pressure for complete infiltration (lowest pressure which leads to fingerwidth divergence), both the fracture stress and the Weibull shape factor increase, which is to be expected as a completely interconnected microstructure is formed.

Figure 6 is a plot of the pore cluster probability for the baseline simulation, with no invasion percolation trapping mechanism operating. These simulations assume the backside of the part is evacuated leaving no incompressible gas phase that would need to diffuse out of the cavity. It is evident upon comparison with the plot for trapping simulations (Figure 4), that the largest pore clusters are much more readily removed at lower pressures when no trapping mechanism is operative. The necessity of conducting multiple simulations at different random number seedings is also clear from Figure 6, as the data was taken after only a single simulation set (compared to eight for Figure 4), and displays some statistical uncertainty. The plot in Figure 7 is the Weibull survival probability plot for the no-trapping baseline simulation. As expected, the maximum allowable stress values are higher because the flaw size distribution is shifted lower. The Weibull shape factor, however, is not significantly better than the trapping case, because the spread in the data is greater due to the smaller sampling size.

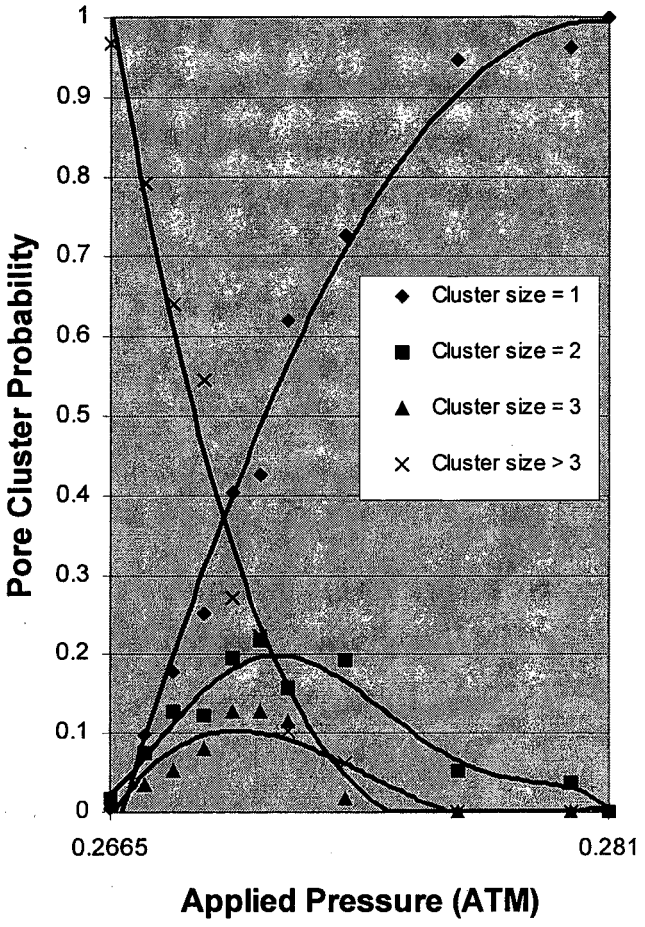

Figure 6 Pore cluster probability plot for the baseline simulation, without the invasion percolation trapping mechanism active. The largest pore clusters are removed at lower pressures.

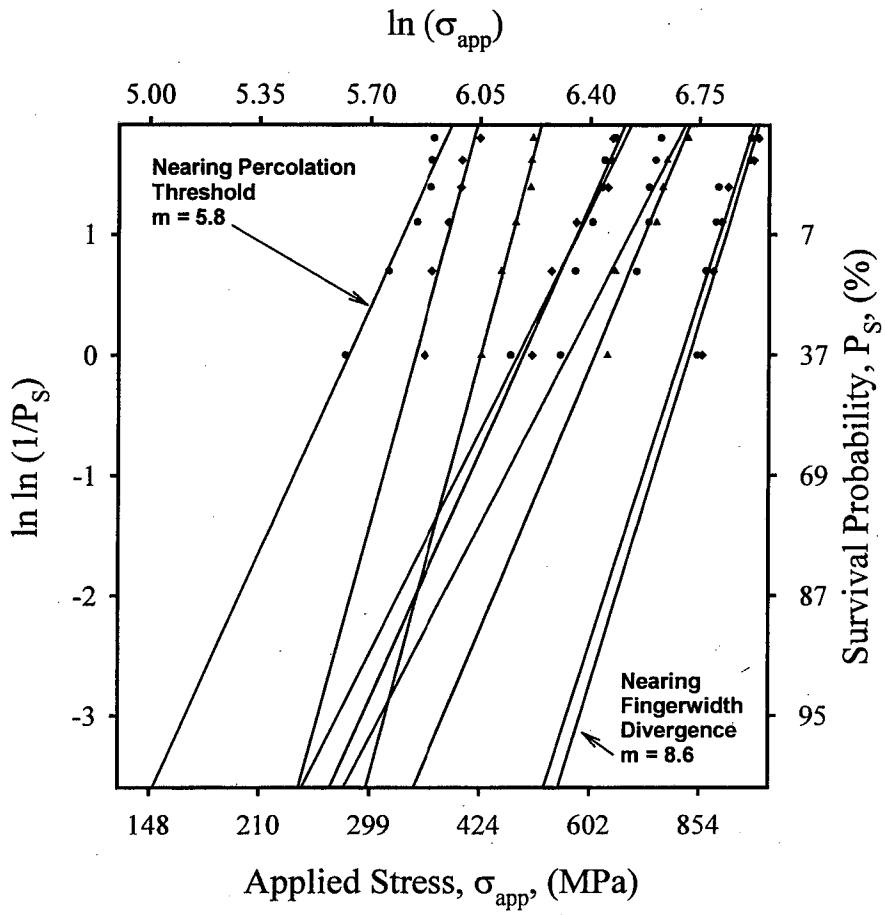

Figure 7 Weibull survival probability plot of the baseline simulation, without invasion percolation trapping mechanism, taken with only one seeding of the random number generator. The spread in the data leads to uncertainty in the Weibull shape factor.

5 Summary

In summary, the baseline simulation, without interface transformation kinetics, has been discussed to demonstrate the critical phenomena present in these systems, and detail the statistical techniques employed to quantify the results. In addition, the difference between simulations conducted with and without the invasion percolation trapping mechanism has been presented. The results presented in Chapter 5 will incorporate interface transformation dynamics in the driving force for infiltration.

[1] Pech-Canul, M.I., Katz, R.N., and Makhlouf, M.M., "Optimum Parameters for Wetting Silicon Carbide by Aluminum Alloys," *Metall. Mater. Trans. A* **31A** 565-73 (2000).
[2] Keene, B.J., Review of data for the surface tension of pure metals," *International Materials Review* **38** 4 157-170 (1993).
[3] Hannon, E.H., and Hornor, J.A., *Proc. ISHM* (1992).
[4] Anderson, T.L., Chapter 2 in *Fracture Mechanics, Fundamentals and Applications*, 2nd ed., CRC Press, Boca Raton (1994).

Chapter Five Simulations of Invasion Percolation with Interface Transformation

1 Introduction

The baseline simulations presented in Chapter 4 illustrated the methodology to be used for the more complex simulations to be discussed now. The only driving force allowed to operate in those studies was an applied pressure, in other words the interface transformation rate was zero. Now an interface transformation provides the primary driving force for infiltration. The magnitude of the rate and the range over which it operates on the contact angle will be coupled with the applied pressure and the effect on the resultant microstructure and mechanical properties observed. Also, a kinetic growth constant determines the rate at which a secondary product phase forms and eventually fills the pore space. When a system spanning cluster of this phase appears, the permeability of the lattice to the fluid source is assumed so small that the infiltration essentially stops. The transformation rate is thus dynamically linked with pore interstitial product phase growth.

2 Application of the Transformation Rate

As mentioned in Chapter 3 the rate at which the interface transforms is related to the evolution of the apparent contact angle with time. Exponential decay of the contact angle with time is typical, but observations of sessile drop studies show that the situation is more complex. Figure 1 schematically indicates what is observed in real material systems. Four regions can be identified in many systems. In region I, surface ahead of the fluid interface saturates with vapor and a precursor film forms. This corresponds to

the surface condition uniformly changing throughout the pore space, without direct contact with the interface. In region II, dissolution of the near surface material occurs, which in the primary system studied here may result in the reduction of surface silicon oxides and the formation of aluminum oxide. This phenomenon is again modeled as occurring without direct contact with the bulk fluid. It is in region III where the interface transformation kinetics are applied. In this region a thin alloy film is forming, corresponding to the stable chemical species present at that temperature. This effect is related to a surface reaction rate constant, and correlates with the reduction in surface contact angle over that region. In the SiC/Al system, thin film X-Ray Diffraction (XRD) studies have correlated the reduction in contact angle in region III to the formation of a thin Silicon-rich alloy on the surface.[1,2] Exponential decay plots have shown good fit to experimental data in this region. Lastly, in region IV the contact angle diminishes much more slowly and product phase growth into the pore space occurs.

The transformation rate is extracted from Figure 1 by fitting exponential decay curves to the experimental data while adjusting the values of θ_i and θ_f, to correlate with surface XRD data. For example, when the Si-rich alloy resulting from the bulk fluid in direct contact with the surface is first detected at time t_i and completely covers the surface at time t_f, a wetting condition on the lattice is established and spontaneous interface advance will occur as the liquid spreads. In the model, this corresponds to the reduction of the apparent contact angle from θ_i to θ_f, and the transformation rate is $R = 1/(t_f - t_i)$. The initial contact angle at which the bulk fluid initially alters the chemistry of the surface will change from system to system, and can have large effects on the resultant microstructure and the time necessary for full infiltration.

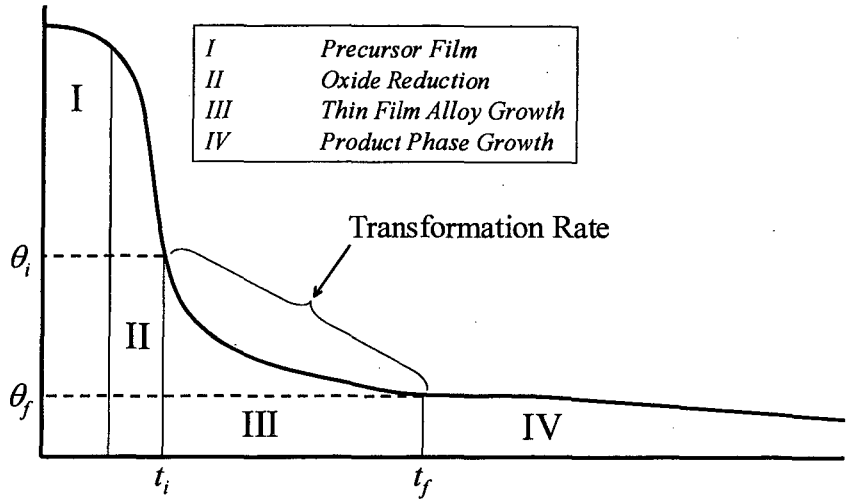

Figure 1 Schematic of the correlation of apparent contact angle with the physical phenomena responsible. The region over which the bulk fluid first alters the surface chemistry is used to extract the interface transformation rate (Region III).

3 *Lattice I* Simulations

3.1 Rapid Transformation Rate, High Kinetic Growth Rate Constant, with Trapping

The transformation rate in these simulations was determined to be 0.225, with θ_i = 60° and θ_f = 40°. The system was modeled after the Al/Si/SiC system studied by Pech-Canul *et al.*[1] and others in which the Silicon content is not sufficient to suppress the formation of interfacial reaction phases. The kinetic growth rate constant was taken to be 0.250 μm^2/minute, corresponding to the rapid growth of the Al_4C_3 phase at low to intermediate temperature. The lattice studied was *Lattice I*, discussed in Chapter 4 for the baseline simulations. Figure 2 shows the pore cluster probability and Weibull failure probability plots for this simulation.

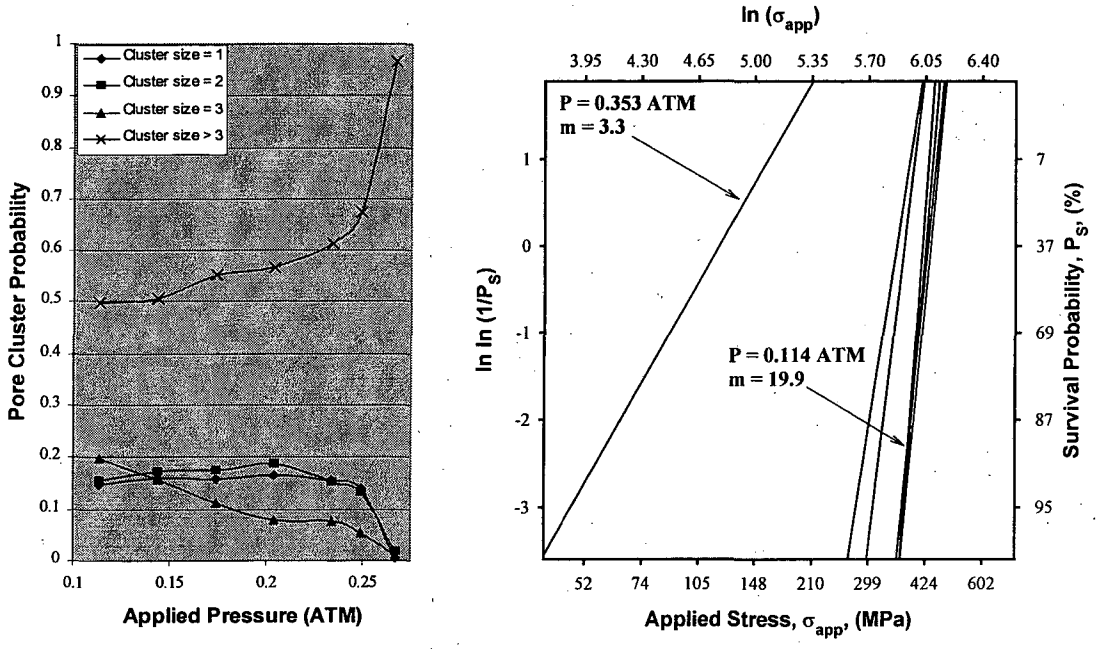

Figure 2 Pore cluster probability and Weibull failure probability for transformation rate R = 0.225 and kinetic growth rate constant k = 0.250. The Weibull shape factor m decreases with increasing applied pressure, indicating a higher degree of capillary fingering-induced residual porosity.

In comparison to the baseline simulation presented in Chapter 4, the incorporation of interface transformation dynamics has produced a range of microstructures over a much wider range of pressures. The mechanisms described in Chapter 2 are quite evident here. At low pressures, the pore space is filled uniformly as the transformation drives flow. At higher pressure, capillary fingering becomes the primary effect, leading to a rough interface and large pores. In addition, two features are worth mentioning as they are representative of all the simulations with transformation dynamics employed. First, there is no absolute divergence of the fingerwidth at a finite critical pressure. Second, an

effective percolation threshold pressure is identified, to include the effects of the interface transformation on the system.

These phenomena can be explained by referring to Figure 3, which shows microstructures from an intermediate pressure in (a), where the system is approaching the time at which a system-spanning cluster of interfacial product phase first forms, and from a higher pressure in (b), where the interface transformation operates just enough to allow the applied pressure to span the lattice. In (a), it is clear that the time required for the complete divergence of the fingerwidth at lower applied pressure would be well past the point of pore space closure due to plugging of pore throats at the fluid entry point by product phase. From the microstructure in (b), an effective percolation threshold can be defined, which describes the pressure at which the system forms a singular system-spanning pore at the given transformation rate. The system in (a) was simulated at 362 minutes to completion, whereas the simulation in (b) took only 0.1 minutes. Thus the effective percolation threshold is determined as the lowest pressure at which the initial transformation events, i.e. events occurring to assist the entry into the lattice by the infiltrate, initially enable a system-spanning cluster. The times in these systems are therefore not physically meaningful, as they violate the assumption of quasi-static flow. Some other means of determining simulation time would be needed, e.g. an application of Darcy's Law. Obviously the microstructure in (b) is undesirable, the fracture strength was found to be below 50 MPa (see Fig. 2). Nevertheless, the simulation is useful because it provides a bound for the quasi-static flow assumption.

The optimum microstructure for this simulation was found to be the one shown in Figure 3a, simulating an applied pressure of 0.248 ATM (3.6 psig). The total residual

porosity was found to be 14.1 % (relative to original porosity). From Figure 2 the Weibull shape factor was determined to be 12.2 with a survival probability of 98% predicted at an applied pressure of approximately 275 MPa. The higher values for fracture stress and Weibull modulus for the simulations run at lower pressures are deemed non-physical at this system size, because of the formation of a core-shell morphology at this high transformation rate. These systems would not have come to complete infiltration.

(a) (b)

Figure 3 Best case (a) and worst case (b) microstructures for the simulation described in Section 3.1. The formation of a secondary reaction phase is evident near the fluid entry point in (a).

3.2 Modifying θ_i

Since the interface transformation rate is extracted from the plot of the apparent contact angle evolution over the range when the bulk fluid is in direct contact with the lattice, the initial contact angle plays a large role in the overall time required for the transition to the wetting state in the porespace. The next simulation to be discussed

increases the initial contact angle from 60° to 75°, all else being equal. Physically, this also corresponds to the formation of another thin film alloy that is partially wet by the advancing fluid front, thermodynamically stable at the higher temperature. In the system studied here, for instance, this could correspond to the compound Al_4SiC_4, which forms at a higher temperature than Al_4C_3. The pore cluster probability and Weibull survival probability are given in Figure 4.

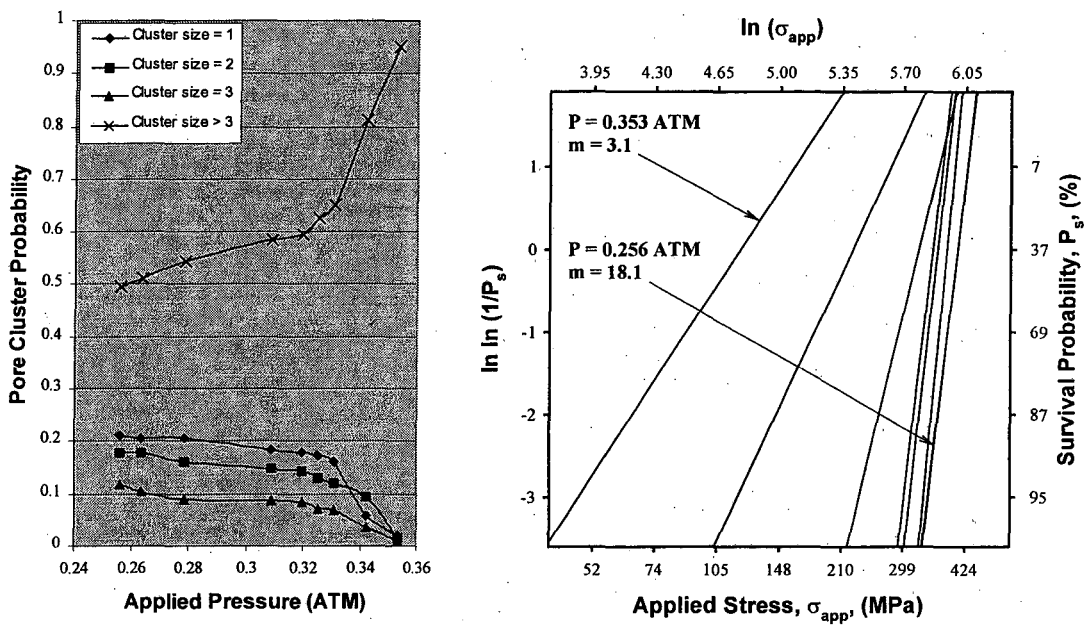

Figure 4 Pore cluster probability and Weibull survival probability for $R = 0.225$, kinetic growth rate constan $k = 0.250$, with $\theta_i = 75°$, simulating a higher temperature process.

Comparison with the results from the earlier experiment, with $\theta_i = 60°$, indicates lower strengths and Weibull shape factors at the increased temperature. The optimum simulation was found to be 0.3310 ATM applied pressure, a higher pressure than the previous case. This is expected as the system transforms faster and thus the growth of interfacial product phases commences earlier. Correspondingly, the threshold percolation

pressure for these simulations (pressure at which system spanning initially occurs without transformation) is shifted higher. At low pressures the growth of secondary phases in the pore space became the primary feature of the simulation. The strength of the best case microstructure was found to be 215 MPa with a Weibull shape factor of 8.9. The higher strength microstructures in Figure 4 at lower pressures were deemed non-physical (at this system size) because the pore space was sealed due to the shell formation. They would however be attainable in the event the product phase growth constant is sufficiently low.

3.3 Modifying the rate R

Another means of simulating the rate of transformation is found in the transformation rate R itself. Whereas changing θ_i incorporates the effect of compositional differences in the thin film alloys at different temperatures, the rate R itself enables the incorporation of other phenomena that can alter the wetting transition. These include alloying additions to reduce surface tension and surface pretreatment to increase the reaction rate and thus the rate of spreading of the fluid. The simulations (from Lattice *I*) shown in Figure 5 are for transformation rate $R = 0.200$, with kinetic growth rate constant $k = 0.250$. The optimum microstructure was found to be at $P = 0.249$ ATM, where the strength was approximately 225 MPa and the Weibull shape factor was 11.2. The residual porosity (relative to initial porosity) was 15.0 %. Microstructures obtained from lower applied pressures were deemed non-physical.

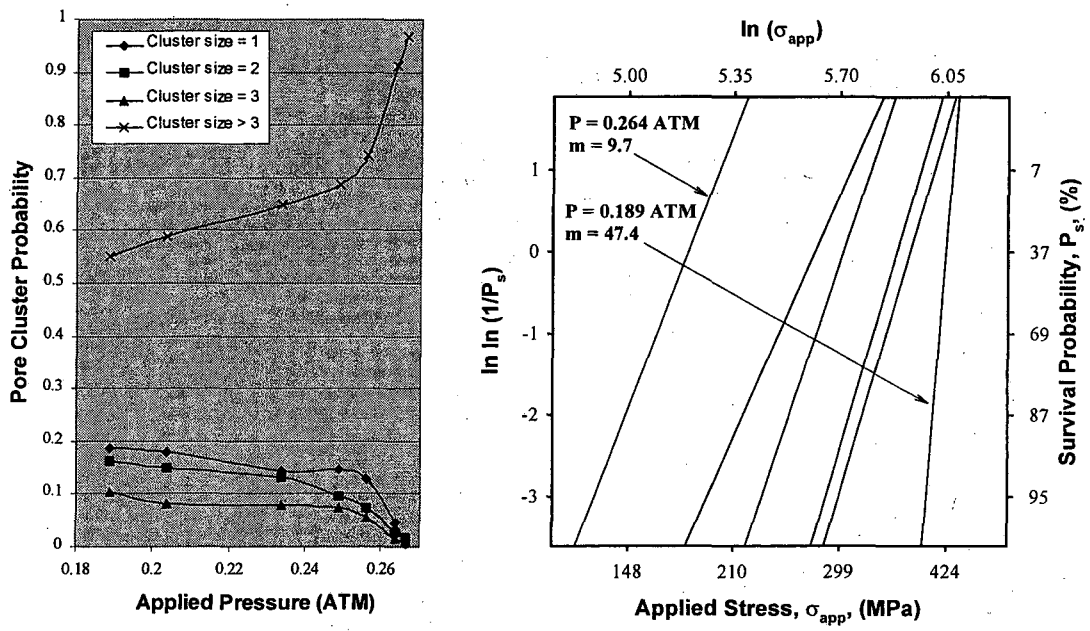

Figure 5 Pore cluster probability and Weibull failure probability for the simulations with $R = 0.200$, $k = 0.250$.

The next simulation set conducted on Lattice *I* had a slower transformation rate $R = 0.175$, with $k = 0.250$ μm^2/min. The results are summarized in Figure 6. The optimum microstructure occurred at P = 0.250 ATM, which upon examination of Figure 6, is the point where the probability of pore cluster size 1 attains approximately 80% its maximum value, and the probability of large pore clusters (> 3) begins to diverge rapidly to unity. The strength at 98 % survival probability was 250 MPa, with a Weibull shape factor of 14.1. In the simulations with $R = 0.225$, $R = 0.200$, and $R = 0.175$, all with optimal microstructures at applied pressures very near 0.250 ATM, the best microstructures (without shell formation) with the highest Weibull moduli, occurred when the ratio of the probability of pore cluster size 1 to pore cluster size > 3 was maximum. It is concluded

from the data that the more rapid transformation rate produced the best microstructures with the highest mechanical reliability with respect to fracture. This is consistent with what is known about the positive effect surface-activating wetting agents have on infiltration rate.

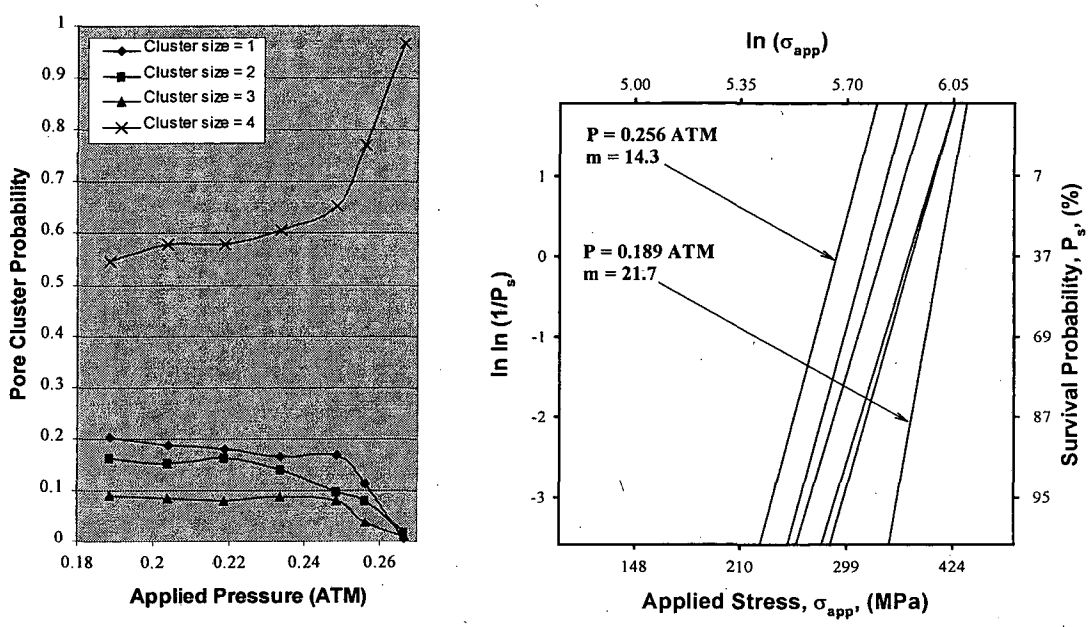

Figure 6 Pore cluster probability and Weibull failure probability for R = 0.175, k = 0.250.

3.4 Modifying the Kinetic Growth Rate Constant *k*

In the simulations discussed thus far, the kinetic growth rate constant was set at 0.250 μm^2, and the transformation rate R and initial contact angle θ_i adjusted. Reducing the value of k can simulate suppression of interfacial product phase formation. There are two ways this can be envisioned; 1) the addition of an alloying element and/or processing in an atmosphere that suppresses the interfacial reaction; and 2) a reduction in k due to a lower processing temperature. For example, adding Silicon to the Aluminum alloy at 20

weight percent will suppress the formation of Al_4C_3. In these simulations, the resultant microstructure (residual pore size distribution) does not change, only the time for the formation of the system-spanning cluster of product phase. Thus the assumption is made again that the reduction in pore space permeability does not starve the interface during chemical reaction-controlled infiltration until the pore space is completely plugged. Referring to Figure 2, with $k = 0.05$ μm^2/min., the optimal microstructure was obtained at the lower pressure of 0.22 ATM, which allowed for more uniform interface growth. The 98 % survival probability strength is increased to over 350 MPa, with the Weibull shape factor increasing to 20. The Monte Carlo time for completion of the simulation was 550 minutes.

3.5 Simulations without Trapping Mechanism

Without the invasion percolation trapping mechanism most of the pores of size greater than one were removed. Figure 7 displays the results for the three simulations already mentioned, with variable transformation rate R, and $\theta_i = 60°$. Fingerwidth statistics were employed because they were a more sensitive indication of the variation in residual porosity than the residual pore size distribution, from which the data could not be treated on a statistically significant basis. The fingerwidth diverges rapidly at pressures less than 0.2665 ATM, which is the percolation threshold pressure for *Lattice I*. At the threshold pressure, individual transformation events on the lattice produce rough interface growth patterns that are governed by the local lattice geometry. At pressures below the threshold pressure, the lattice must transform more to advance the interface, resulting in a more wetting condition. More uniform growth patterns result from a higher relative occurrence of menisci overlap mechanisms. At pressures above the percolation

threshold pressure p_c, capillary fingering would dominate flow when trapping of a immiscible phase occurs. The fingerwidth would decrease and the mechanical properties of the resulting microstructure would worsen. Without the trapping mechanism, i.e. simulating processing in vacuum, at pressures above p_c the fingerwidth increases until the critical pressure for divergence of the fingerwidth is reached. This occurs over a very narrow range of applied pressure, as in the baseline simulations discussed in Chapter 3. These simulations are deemed non-physical because they occur at vanishing small times that would violate the assumption of quasi-static flow in pore throats. In effect, during these simulations the lattice is fully infiltrated without an interface transformation at all. Therefore, this regime of the simulation was not investigated. The effect of the homogeneity of the starting lattice on the pressure range over which the divergence of the fingerwidth occurs will be discussed later.

The scarcity of large pores leads to improved mechanical properties, as seen in Figure 7. A best case microstructure, occuring at a pressure of 0.252 ATM, had a Weibull modulus of over 20 and a 98 % survival probability of over 550 MPa. This may exceed the failure stress of the matrix material in many metal/ceramic composites, in which case the flaw size distribution inherent to the matrix must be considered. As mentioned earlier, the small volume of residual porosity data makes identification of an effective trend from a single simulation run problematic. The best case microstructure was chosen as the one with the highest fingerwidth that had not yet formed a system-spanning shell cluster. This simulation came to completion with a Monte Carlo transformation time of 427 minutes.

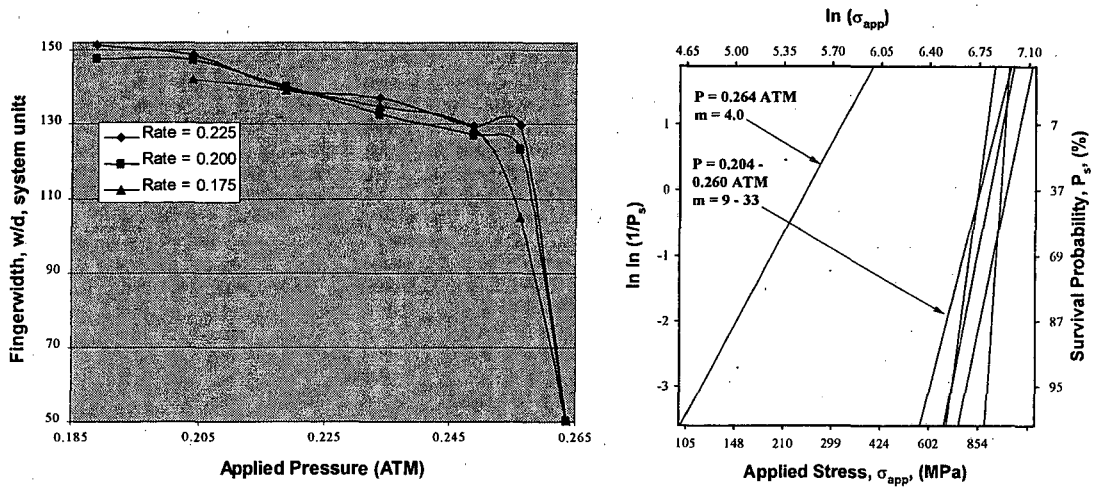

Figure 7 Fingerwidth and Weibull failure probability plot for the simulation without the invasion percolation trapping mechanism operative. The Weibull plot was taken from the simulation with $R = 0.200$.

4 *Lattice II* Simulations

One of the most useful features of co-interpenetrating composites is the ability to tailor the material properties for the specific application of interest. Higher thermal conductivity, for example, can be achieved by increasing the amount of metal phase relative to the ceramic matrix. As long as a fully interconnected microstructure of percolating metal phase is maintained, the desired thermal properties can be predicted. Three systems simulated using *Lattice II* are discussed below. This lattice, in which the grain size is allowed to uniformly vary from 12.75 to 24 μm, produces an initial matrix porosity of 0.495, much more open than *Lattice I* (porosity 0.327). In going to a larger lattice porosity there is an increase in the capillary length, thus it is possible to maintain

pore level infiltration effects at a higher fluid interstitial velocity (at smaller Monte Carlo times).

4.1 Low Temperature Transformation, Without Trapping

This simulation set was taken with kinetic growth rate constant k = 0.250 μm^2/min., and transformation rate R = 0.225/min. The results are shown in Figure 8.

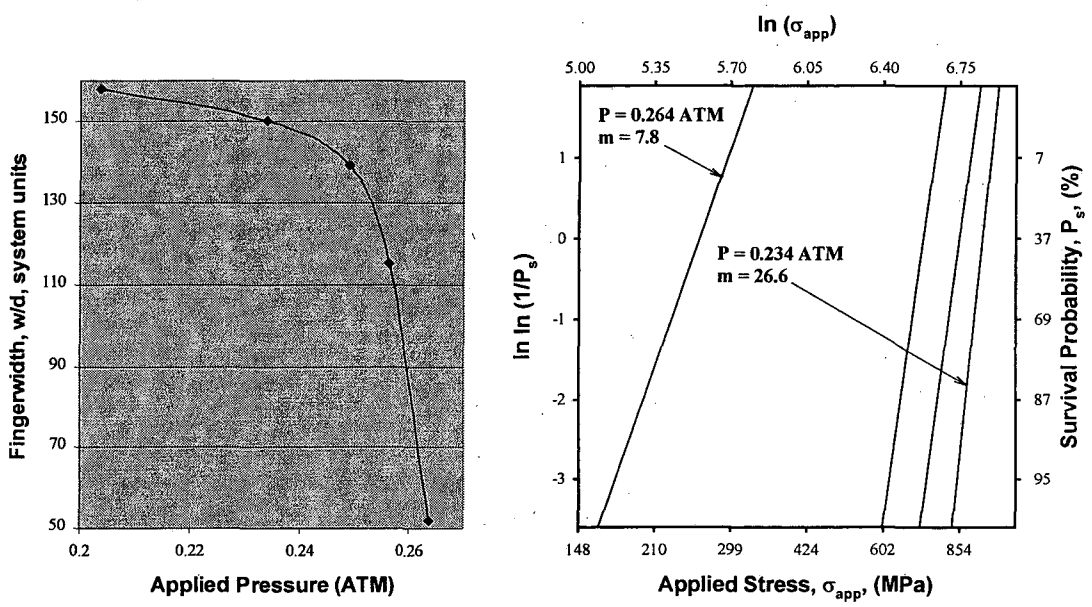

Figure 8 Fingerwidth and Weibull Survival Probability plots for *Lattice II*, low temperature simulation without trapping mechanism.

The best case microstructure was obtained at a pressure of 0.22 ATM, where the fracture strength at 98 % survival probability is 800 MPa. This is an improvement over the best case fracture strength observed for *Lattice I* under these conditions, due to the larger pore throat openings taking longer times to fill with secondary reaction phase. Thus a lower applied pressure was allowed, leading to higher fingerwidths and a more homogeneous residual pore size distribution.

4.2 High Temperature Transformation, Without Trapping

Figure 9 shows the results of this simulation set, with the initial transformation contact angle set at 75°, simulating a higher temperature process. All other parameters were the same as the *Lattice II* simulations of Section 4.1.

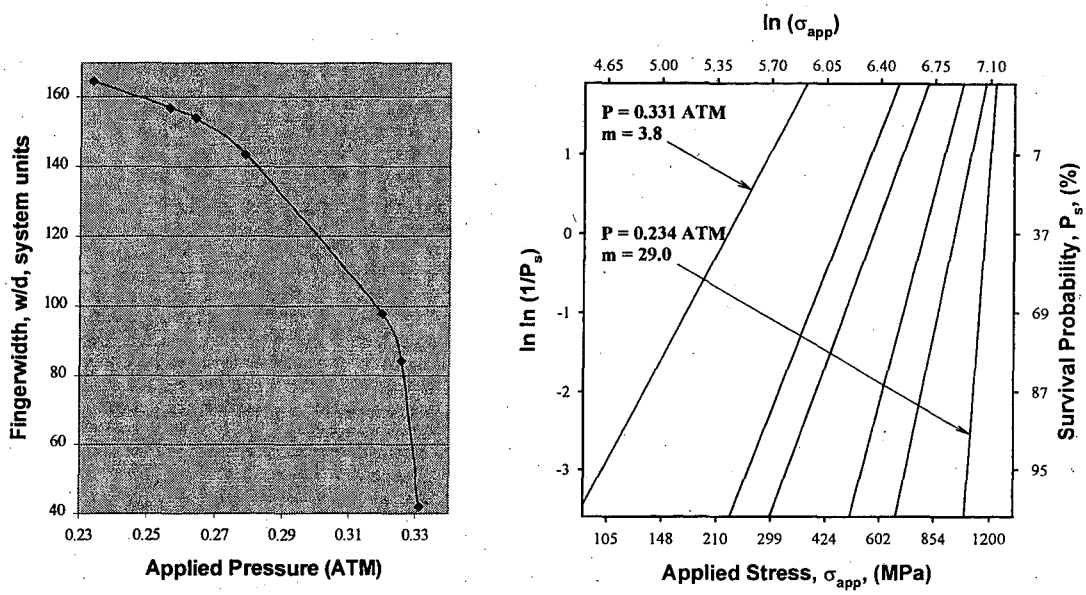

Figure 9 Fingerwidth and Weibull Survival Probability plots for *Lattice II*, high temperature simulation without trapping mechanism.

The best case microstructure in these simulations was found at an applied pressure of 0.275 ATM, where the fracture strength at 98 % survival probability was 475 MPa and the Weibull shape factor was 7. Higher strength microstructures processed at lower pressures were deemed non-physical due to the formation of a core-shell morphology. Clearly the mechanical properties of the lower temperature simulations are superior, as they can be processed at lower pressure.

4.3 Low Temperature Transformation, With I/P Trapping Mechanism

The results presented in Figure 10 represent low temperature transformation on *Lattice II*, with kinetic growth rate constant $k = 0.05$, and transformation rate $R = 0.225$. The best case microstructure occurred at a pressure of 0.204 ATM, where the 98 % survival probability strength was 215 MPa and the Weibull shape factor was 8. Higher strength microstructures obtained at lower applied pressures were deemed non-physical due the formation of core-shell morphologies, but might be significant at lower values of the kinetic growth rate constant k.

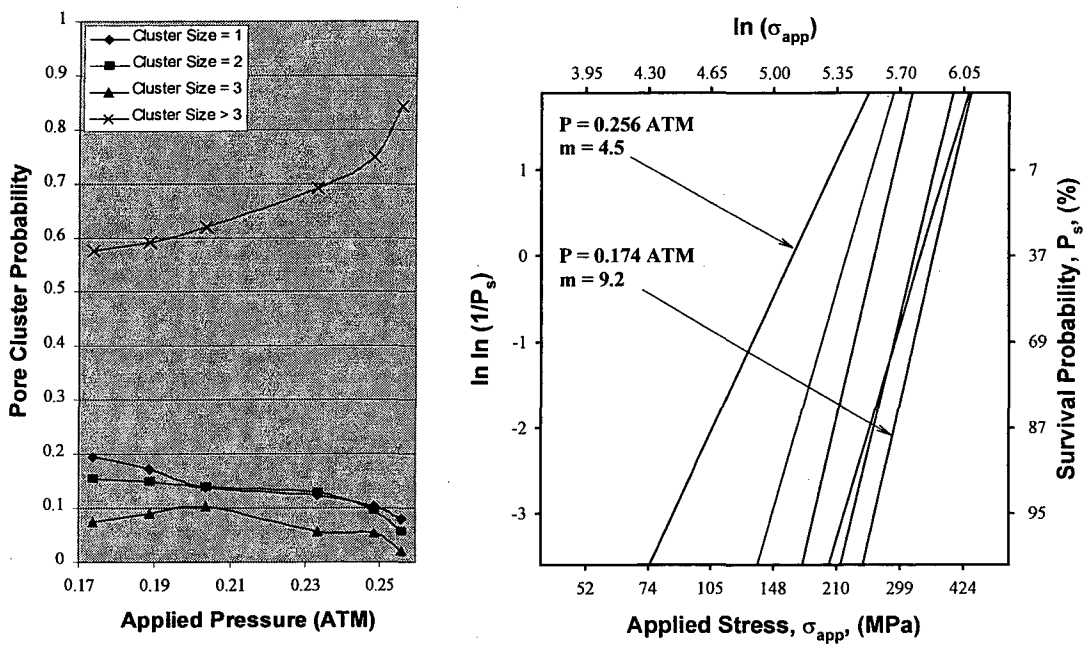

Figure 10 Fingerwidth and Weibull Survival Probability plots for *Lattice II*, low temperature simulation with I/P trapping mechanism.

5 Process Maps

The process maps discussed below are useful experimentally because they condense the information obtained from individual studies into a format that can be utilized when designing process parameters. The maps are read topographically, along lines of constant fingerwidth or fracture strength. The applied pressure and transformation rate make up the dependent variables. The lattice porosity and process temperature are in most instances held constant. Areas shaded on the map represent processing conditions leading to the formation of core-shell morphologies. Two product phase growth rates are indicated. All microstructures obtained at pressures less than those indicated by the boundary line are deemed non-physical at the system size studied (1 cm), as they were infiltrated at long times, leading to pore space closure with reaction phase. For example, all microstructures to the left of the line marked $k = 0.250$ are disallowed, however, for the slower growth rate the microstructures between this boundary and the boundary line $k = 0.05$ are accessible. All states to the left of the $k = 0.05$ boundary line are inaccessible. In addition, the maps are bounded at a pressure that is the limiting pressure of the capillary length criterion. At pressures above the highest pressures shown on the maps the interface would move so rapidly as to violate the assumption which allows for the pore-level analysis being conducted. A direct correlation of fingerwidth, a measure of the degree of capillary fingering effect, and fracture strength is evident. A co-interpenetrating composite material with a high fingerwidth is more homogeneously infiltrated than one with a lower fingerwidth.

5.1 Low Temperature Transformation with Trapping Mechanism

The process maps for the simulations describing low temperature transformation, with the invasion percolation trapping mechanism, are shown in Figure 11. The best microstructures accessible from the simulations are those with the transformation rate R = 0.225 min. $^{-1}$, k = 0.05 μm^2/min., and pressures no less than 0.215 ATM. For the higher kinetic growth rate constant, more microstructures become inaccessible at lower pressures. Thus higher pressures are required to complete the infiltration before the core seals off. This leads to increased capillary fingering, lower fingerwidths, and lower fracture strength values.

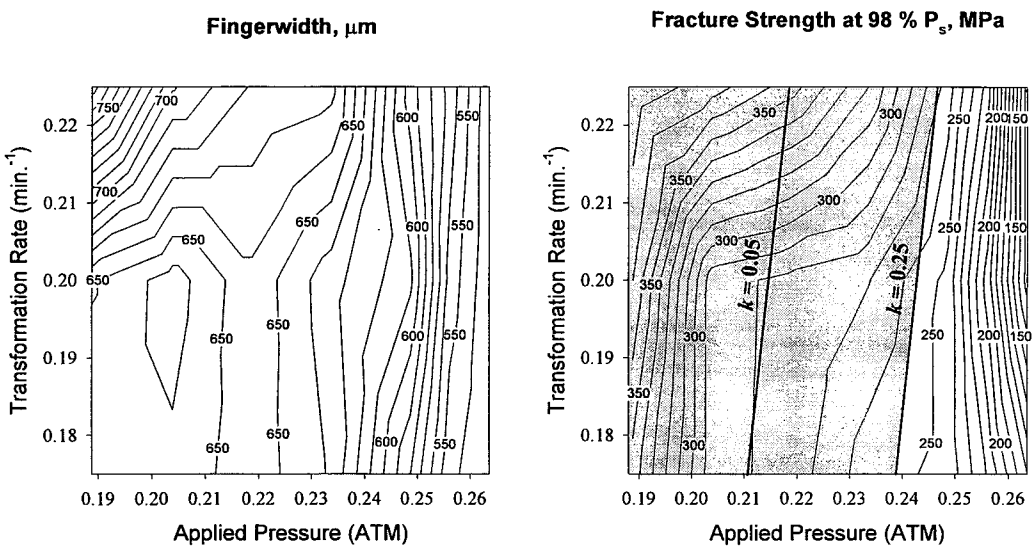

Figure 11 Process maps for low temperature transformation with invasion percolation trapping mechanism. The constant parameters were θ_i = 60°, the initial transformation contact angle (a function of temperature), and the initial lattice parameters found in Lattice *I*, with a porosity of 0.327.

5.2 High Temperature Transformation with Trapping Mechanism

Figure 12 shows the process maps for the simulations encompassing high temperature transformation, with the invasion percolation trapping mechanism. Higher pressures and lower times were required to infiltrate these systems because of the longer time period of reaction, resulting in more product phase growth. The result is lower fingerwidths and lower fracture strengths than the lower temperature simulations.

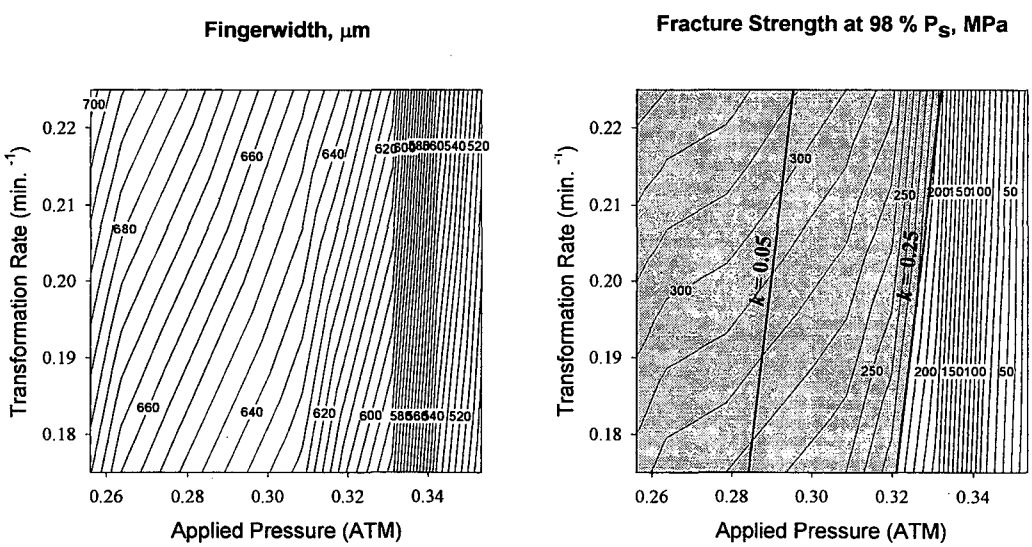

Figure 12 Process maps for high temperature transformation with invasion percolation trapping mechanism. The constant parameters were θ_i = 75°, the initial transformation contact angle (a function of temperature), and the initial lattice parameters found in Lattice *I*, with a porosity of 0.327.

5.3 Low Temperature Transformation without Trapping Mechanism

The process maps shown in Figure 13 represents the simulations of low temperature transformation, without the invasion percolation trapping mechanism active.

As mentioned earlier, this would physically correspond to evacuating the backside of the workpiece during infiltration. It is clear that high strength microstructures are attainable from these simulations, provided the applied pressure is below 0.26 ATM. The strengths obtained by these analyses imply that near-theoretical conditions apply. In these cases the flaw size distribution of the matrix material would limit the strength of the microstructure. In this model it is assumed the flaw initiation point occurs in an un-infiltrated section of the initially porous matrix material.

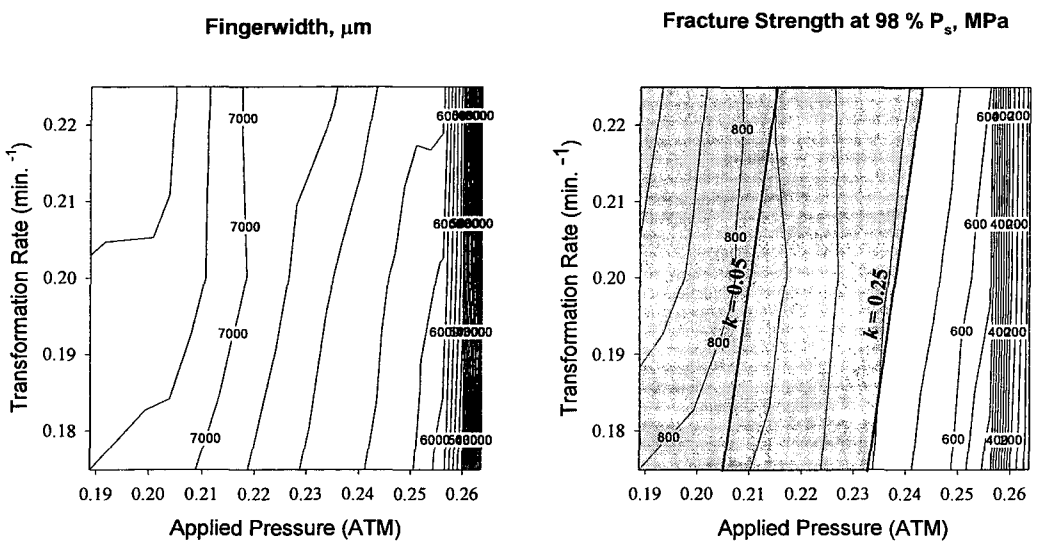

Figure 13 Process maps for low temperature transformation without the invasion percolation trapping mechanism. The constant parameters were θ_i = 60°, the initial transformation contact angle (a function of temperature), and the initial lattice parameters found in Lattice *I*, with a porosity of 0.327. The fracture strength would be determined by the initial flaw size distribution within the bulk of the ceramic matrix.

5.4 Low Temperature Transformation without Trapping Mechanism, *Lattice II*

Figure 14 presents the process maps for the simulations run on *Lattice II*, with initial porosity ϕ = 0.495, at low temperature, with kinetic growth rate constant k = 0.250 μm^2/min. Two transformation rates were studied, R = 0.225 and R = 0.175. The main feature to note is the absence of disallowed regions on the map, over the pressure ranges of interest. The larger pore size enables the infiltration to come to completion with very high fingerwidths before the pore space seals off. Simulations on *Lattice II* are thus designed to study higher metal concentration composites.

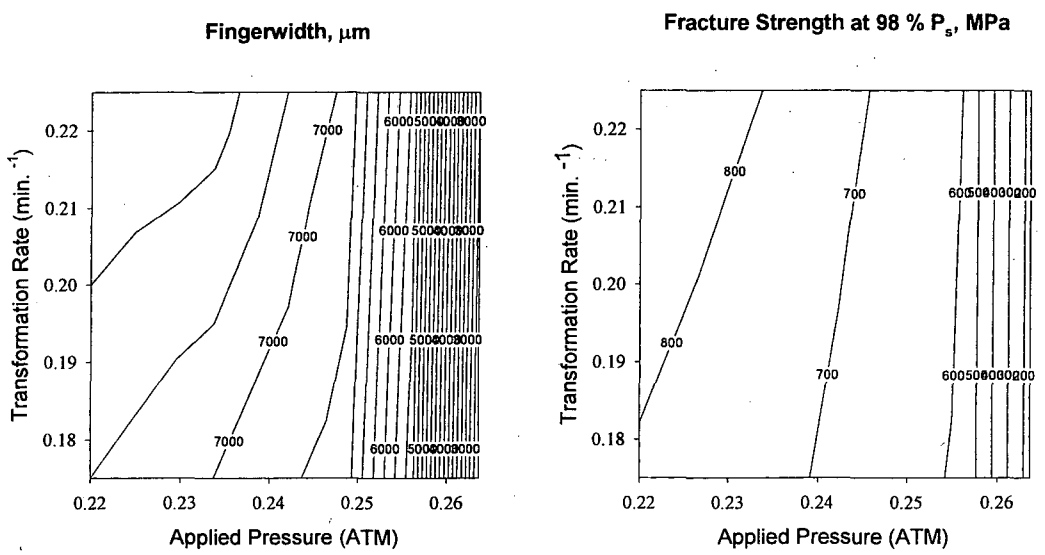

Figure 14 *Lattice II* process maps for low temperature transformation without the invasion percolation trapping mechanism. The constant parameters were θ_i = 60°, the initial transformation contact angle (a function of temperature), and the initial lattice parameters found in Lattice *II*, with a porosity of 0.495. There are no disallowed regions on the map over the pressure range of interest.

5.5 Effect of Processing Temperature

Figure 15 shows the results obtained during *Lattice II* simulations without trapping, in which the initial transformation contact angle was allowed to vary from 60 to 75 degrees. As mentioned previously, this corresponds to the change in composition of a thin film alloy on the surface at different temperatures. In the Aluminum/Silicon Carbide system, for example, at high temperatures the compound Al_4SiC_4 forms, while at lower temperatures the compound Al_4C_3 forms. Therefore simulations of this type are designed to demonstrate the effect of varying the temperature on the resultant microstructure and mechanical properties.

Examination of the process maps reveals that the higher temperature process produced slightly better mechanical properties, at least over the allowed range of pressures indicated. With larger pore openings, even the higher molar volume phases forming at high temperature cannot seal the pore space off completely. Higher fingerwidths and the concomitant higher strength values are the result of the more highly transforming conditions. This is in contrast to the simulations run on *Lattice I*, with a more closed initial porosity, where core-shell morphologies dominated the microstructures obtained at high temperature. It should be noted that the microstructures obtained at low temperature and pressures below 0.22 ATM (lowest pressure seen in Figure 15) showed strengths converging on the high temperature values shown, but would take longer times to complete. At the value of the kinetic growth rate constant k = 0.250, these simulations were non-physical, but at lower k values could be significant. Data was not taken at lower pressures for the high temperature simulations, since near complete divergence of the fingerwidth was observed at 0.22 ATM. The lower pressure

simulations consumed vast amounts of the available CPU time, so were avoided when fingerwidth divergence was observed.

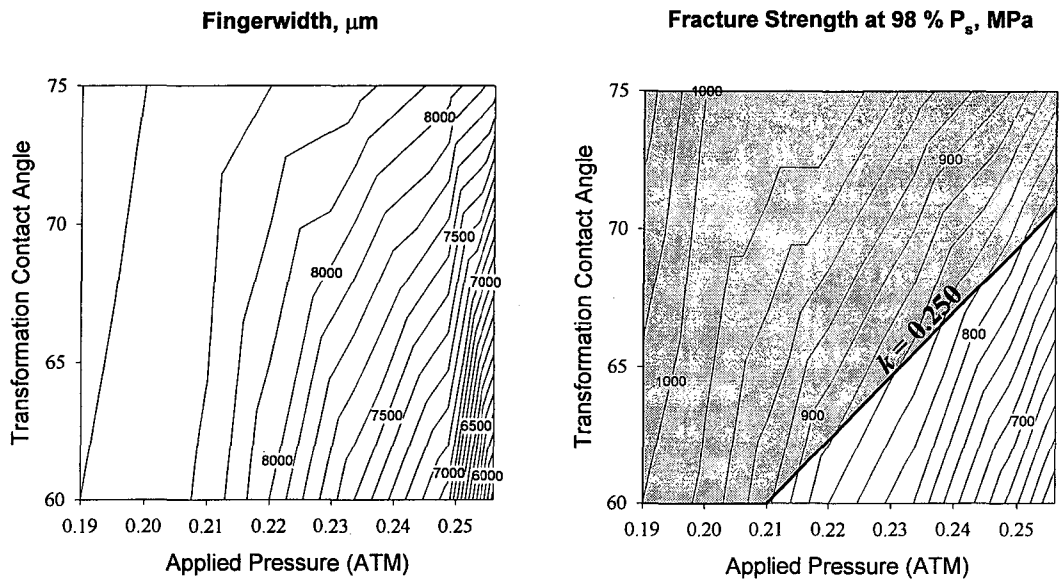

Figure 15 *Lattice II* process maps showing the effect of initial transformation contact angle (a function of processing temperature) for transformation without the invasion percolation trapping mechanism. At pressures above the upper limit shown, the lower temperature case exceeds the quasi-static flow limit. The shaded area represents the regime of disallowed microstructures due to the formation of a core-shell morphology at the given value of the kinetic growth rate constant.

5.6 Effect of Initial Matrix Porosity

The effect of initial matrix porosity is mapped in Figure 16, which shows simulations with the invasion percolation trapping mechanism, *Lattice I* (ϕ = 0.327) versus *Lattice II* (ϕ = 0.495). For both sets of simulations the transformation rate R was 0.225/min., kinetic growth rate constant k was 0.050 μm^2/min. and the initial transformation contact angle θ_i was 60

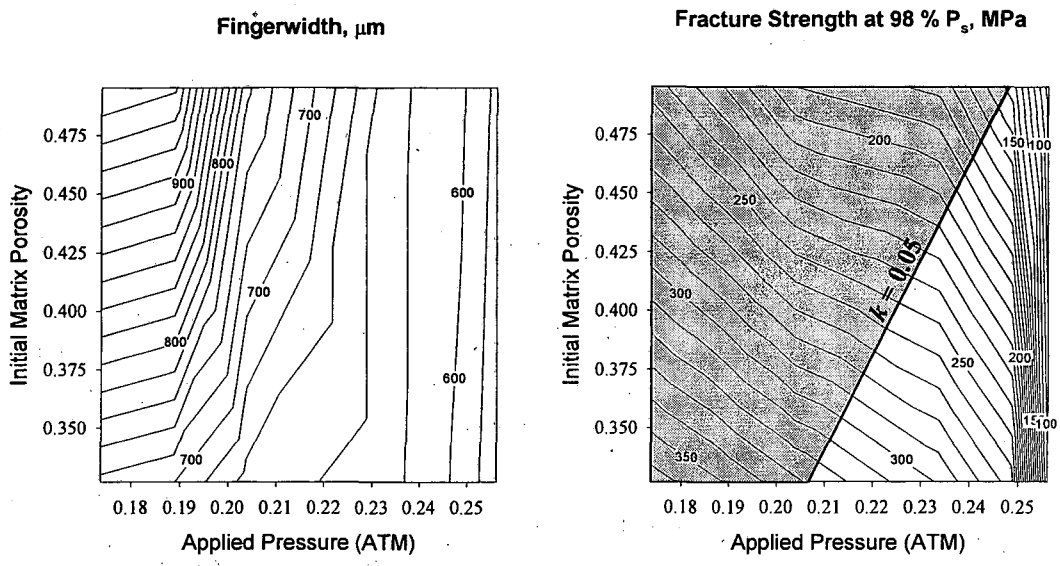

Figure 16 Process maps of initial matrix porosity versus applied pressure for low temperature transformation (with I/P trapping mechanism), and transformation rate R = 0.225.

The best case microstructures were obtained from *Lattice I* at low relative pressure. The most interesting feature revealed by these process maps is that the strength values do not show significant correlation with fingerwidth. The data showed that the fingerwidth values for *Lattice II* (high initial porosity) were higher than for *Lattice I* (low initial porosity), whereas the strength, and especially the Weibull shape factor, was higher for *Lattice I*. This seeming discrepancy can be resolved by looking at the pore cluster probabilities shown in Figure 17, which shows the probability of large pore clusters dominating the microstructure in *Lattice II* over the pressure range of interest. It can be concluded that even though the overall fingerwidth is higher in *Lattice II*, the strength is determined by the probability of finding large pore clusters. The higher fingerwidth values for Lattice *II* are probably due to a more evenly dispersed residual

porosity from the higher occurrence of Invasion-Percolation "overlap" mechanisms when the transformation is completed at longer times.

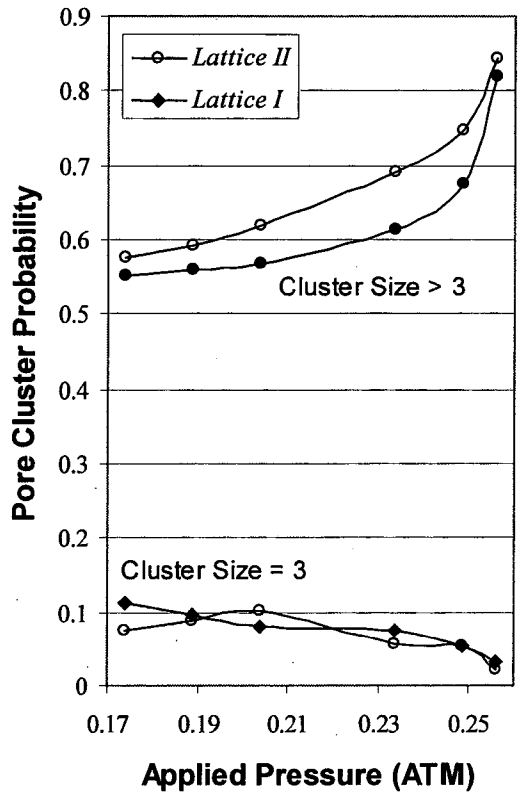

Figure 17 Pore Cluster Probability for large pore clusters, Lattice *I* versus Lattice *II*, demonstrating that good mechanical integrity is more accurately correlated with pore cluster size, and not fingerwidth.

The discrepancy is again evidenced in Figure 18, which shows the microstructures obtained for *Lattice I* and *Lattice II* at an applied pressure of 0.234 ATM. In both cases the average fingerwidth was measure at 630 μm. The residual porosity for *Lattice I* was measured at 0.123, and 0.132 for *Lattice II*. The Weibull shape factor for the *Lattice I*

simulation was 15 with a 98 % survival probability strength of 300 MPa. For *Lattice II* these values were 9 and 190 MPa.

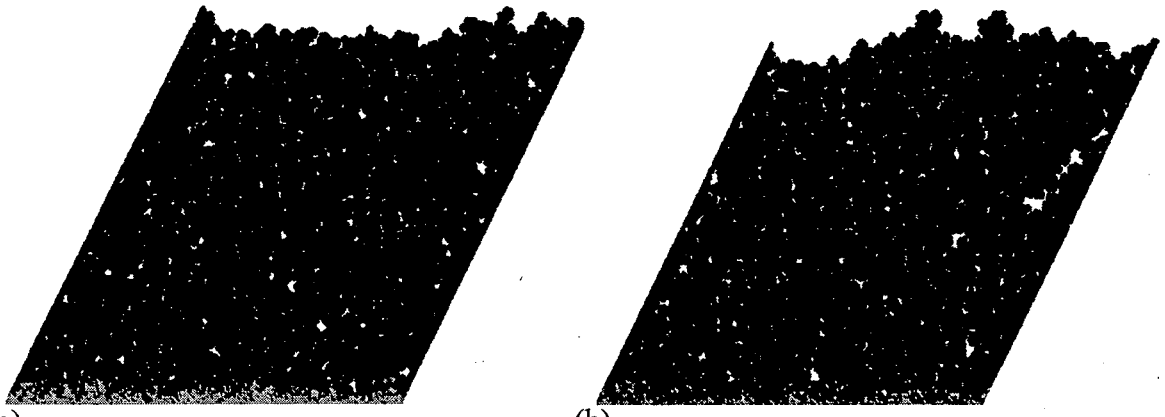

(a) (b)

Figure 18 Microstructures obtained for *Lattice I*, which had a Weibull shape factor of 15, (a); and *Lattice II*, in which the shape factor was 9, (b). Although the fingerwidth was the same for both simulations, the mechanical properties were determined by the appearance of larger pore clusters in *Lattice II*. More pore space closure at the fluid entry point is evidenced in *Lattice I*, with smaller initial pore throat openings.

---

[1] Pech-Canul, M.I., Katz, R.N., and Makhlouf, M.M., "Optimum Parameters for Wetting Silicon Carbide by Aluminum Alloys," *Metall Mater. Trans. A* **31A** 565 (2000).

[2] Laurent, V. Rado, C., Eustathopoulos, N., "Wetting kinetics and bonding of Al and Al alloys on α-SiC," *Mater. Sci. Eng. A* **205** 1-8 (1996).

1 Adjustable Parameters

The following table represents the adjustable parameters in the model used to simulate the reactive infiltration of porous ceramics by molten metals to form a co-interpenetrating microstructure. It illustrates what the physical phenomenon being simulated is dependent on, e.g. composition, temperature, etc. It also indicates by what means the numerical values input to the model were selected. Although the model could be applied generally to any reactive system where enough empirical data were available, in most of the simulations described in this work it was applied to the Aluminum/Silicon Carbide system.

R	θ_i , θ_f	***k***	***P***	***r***
Surface transformation rate	Apparent contact angles for surface transformation	Kinetic product phase growth rate constant	Applied viscous pressure	Lattice grain radii
f(surface pre-conditioning, composition)	*f*(temp., composition)	*f*(temp., processing conditions)	Cannot violate capillary length assumption	Determines initial pore size distribution
Empirical data of the apparent contact angle	Correlation with XRD data	Kinetic growth rate studies	Menisci radius of curvature in pore throat	Initial particle packing, cure rate of amorphous ceramic

Table 1 Illustration of the variable parameters used in the novel invasion percolation model to simulate the infiltration of a co-interpenetrating ceramic matrix composite.

2 Primary Effects

2.1 Applied Pressure

Two main effects obtaining to the applied viscous pressure were observed. First, the times to completion of the simulations were reduced as the pressure was increased. This was one of the primary methods for reducing interstitial product phases (the other being an increase in the transformation rate or reaction rate). Simultaneously there was an increase in residual porosity due to capillary fingering, especially in the simulations with the Invasion Percolation trapping mechanism. At some lower bound to the pressure the process became untenable, even with zero product phase growth, due to the extreme times necessary. Second, at some upper bound to the pressure the assumption of quasi-static flow was violated, thus these simulations were deemed non-physical. The criteria for determining the upper bound was derived from analysis of the capillary length discussed in Chapter Two. If the system size became comparable to the capillary length (which depended on the porosity and pore throat/body ratio) the viscous drag on the interface was surmounted and channel flow would have commenced in the largest pore passages. Then all the pressure would have been dropped in the channel and the pore-level physics would have been lost.

2.2 Transformation Rate

For the system under study, it was observed for all simulations that the transformation rate $R = 0.225$ minute $^{-1}$ was optimal. At much higher rates, for example 0.415 was attempted, product phase growth in the pore space occurred at relatively short

times. This transformation rate was also not physically meaningful in that it could not be accurately extracted from empirical data using an exponential curve fit. Of the three physically meaningful rates studied, (0.175, 0.200, 0.225) it was concluded that the more rapid rate corresponded to a surface condition where wetting and spreading of the liquid phase was assisted, either through alloying to lower the surface tension, or through a reactive wetting process between a pretreated surface and the alloy. The end result was improved mechanical properties due to a more homogeneous residual pore size distribution.

2.3 Initial Transformation Contact Angle

Two initial contact angles were studied, 60° and 75°. The lower angle simulated an alloy forming at lower temperature, such as Al_4C_3 in the system studied here. At 75° another thin film alloy in the Al/SiC system forms at higher temperature, Al_4SiC_4. In all cases studied on similar lattices, the lower temperature simulations produced better mechanical properties. The more rapid growth of product phases in the higher temperature simulations excluded the microstructures with good mechanical properties from consideration. The only microstructures deemed physically realistic with good mechanical properties were processed at higher pressure, leading to microstructures with increased capillary fingering and higher residual porosity than the lower temperature cases.

2.4 Kinetic Growth Rate Constant

Two kinetic parabolic growth rate constants were studied, 0.05 and 0.250 $\mu m^2 minute^{-1}$. Although it is normally considered a function of temperature, there are also cases where intelligent selection of minor alloying additions and processing atmosphere can suppress the growth rate. The most general conclusion drawn was that the lower growth rate constants made possible longer times for completion of the process before core pinch-off occurred. Thus lower values of k were desirable under all circumstances.

2.5 Initial Matrix Porosity

Two uniformly distributed pore spaces were compared, *Lattice I* with $\phi = 0.327$ and *Lattice II* with $\phi = 0.495$. Two conclusions can be drawn from this experiment. The most notable conclusion was that the more open porosity and smaller grains in *Lattice II* produced simulations at longer Monte Carlo times and gave rise to a higher relative occurrence of Invasion Percolation "overlap" interactions, which in turn resulted in higher fingerwidths. However, the larger range of porosity found in *Lattice II* resulted in localized regions of large residual pore clusters. These clusters determined the mechanical properties using the Griffith flaw analysis. Thus for mechanical strength and reliability, pore cluster probability plots were most useful. For thermal properties, especially thermal conductivity where a percolating cluster of metal phase is required, the fingerwidth is a better measure. Another conclusion arises from the fact that in lattices with greater initial porosities, such as *Lattice II*, the time required to plug the porespace with product phase is increased. Therefore more microstructures may be accessible, if the long time required to complete the infiltration is not considered prohibitive.

2.6 Invasion Percolation Trapping Mechanism

In addition to the variable parameters discussed above, two parallel simulation sets were studied in most cases. In all cases the simulations without the Invasion Percolation trapping mechanism in use led to more completely infiltrated microstructures. These simulations modeled evacuating the back side of the workpiece. The removal of pore cluster sizes 3 and greater was especially important; at some pressures theoretical strengths were output from the model. Nevertheless, the use of the trapping mechanism proved both useful and informative. It was utilized to establish the model and it's associated growth algorithm and menisci interactions. It established a best case scenario for microstructures, one that did not depend on subsequent reaction and partial filling of pores with secondary phase. It also simulated processing under atmospheric conditions that may be necessary to suppress the growth of interfacial phases or increase the rate of wetting, e.g. under N_2, which can vastly reduce the surface tension of Al/Si/Mg alloys by binding Magnesium as a nitride. Lastly, the simulations with the trapping mechanism enabled a much more thorough examination of the data due to the relative abundance of discrete pore clusters.

Chapter Seven Concluding Remarks

1 Physical Limitations of the Model

1.1 Permeability

It is not reasonable to expect that viscous forces are totally negligible in these reactive infiltration systems. In the model described in this work, as the lattice grains are allowed to grow the permeability would decrease, and thus the velocity of the fluid front. One problem with a continuum approach is accounting for local areas of complete blockage, which would severely restrict permeability to some areas and not others. One approach would be to divide the lattice into columns, and restrict flow to be in the direction of interface advance. The permeability could be determined only from these discrete regions, so areas of complete blockage would stop the flow completely. This is a "bundle of capillaries" type model, which has fallen out of favor in recent years. The model presented in this work assumes that the reduced local permeability is not significant until a completely interconnected section of plugged pores is formed. Thus diffusion is assumed significant enough to compensate for the permeability reduction. The formation of a system-spanning secondary phase constitutes another percolation transition, one that was not studied in detail in this work.

A better approach, utilizing random walk theory, is dependent upon the computational resources available. If the capillary length is known, summing the random walks to a perimeter around each individual meniscus defined by the capillary length would serve to decrease the time necessary for a statistically significant number of random walkers to arrive at the desired point. The permeability of the lattice to this

perimeter could be determined and updated within some time period defined by the Monte Carlo time step. Flow could then be stopped when the permeability was reduced below some threshold value determined by the average interstitial velocity from Darcy's Law.

1.2 Dimensional Dependence of Properties

One of the difficulties with using a 2-D model in an attempt to predict real systems is the dimensional dependence of properties, such as porosity and tortuosity. The Carmen-Kozeny model for permeability in non-reactive systems assumes values for 3-D tortuosity that are between 2 and 3. Also, it is known that the increased interconnectedness of a 3-D system leads to higher values of porosity. For example, in a close packed 3-D array of spheres, the porosity would be higher than that of a close packed array of cylindrical rods. The scale factor relating the 2-D and 3-D porosities is not linear, being much higher for closer packed arrays. Nevertheless, 2-D models can be useful in advancing the state of knowledge on the relationship between the microstructure and the macroscopic properties of a system. In addition, information obtained can serve as a benchmark for the future work conducted on 3-D systems.

Assuming the lattice permeability could be computed with random walk methods, on the predicative level, some scale factor would be required. The tortuosity of a 2-D lattice is in a close approximation 2/3 that of a 3-D lattice, so a scale factor of 1.5 could be applied to the permeability. The porosity is more problematic. If the model is regarded as a random cross-section through a 3-D pack, the porosity could be assumed constant. There is no disk overlap, however, so the system remains too idealized for such

an assumption. The cooperative fluid advance in a more interconnected 3-D lattice would lead to a higher permeability than the corresponding 2-D cross section would indicate.

1.3 Mechanical Properties

To determine more accurately critical flaw sizes a more complex method for the determination of flaw aspect ratios would be needed. Based on the fact that pore cluster sizes 3 and higher were shown to be most detrimental to the strength, an aspect ratio of 3 was assumed for determination of critical flaw size, a conservative number. In addition, the presence of product phase clusters was not accounted for. In effect these clusters were assumed to be pores, further decreasing the 98 % survival strength. Percolation failure models have been developed to simulate fracture dynamics. In these models the system fails when an interconnected crack path first forms. Such models could be adapted and fit to the types of simulations conducted in this work if the failure mechanism is assumed to be shear or distributed damage. One could envision this assumption being valid for high metal content composites.

1.4 Random Number Generation and Precision

In all cases the pore cluster probability and Weibull survival probability have been presented in their raw form, i.e. without approximation or curve fitting. Thus some of the results show statistical variability, especially simulations run without the I/P trapping mechanism due to the smaller sets of data output. As discussed in Chapter Four, as many as eight simulations using eight different seedings of the psuedo-random

generator are required to achieve high precision in the results. This would have enabled the determination of error bars for the Weibull shape factor and fracture strength. Due to limitations of CPU time this was not feasible for the number of experiments conducted. It was necessary, however, to demonstrate this fact and show it's importance for the benefit of future work.

2 Application of Scaling Laws

An attempt was made early in the work to prove a scaling relationship of the residual pore size distribution with the average pore size. If such a relationship could be proved, statistics like those that apply to purely percolative systems would have been useful and true scaling exponents for the correlation length, percolation probability, and average cluster size could have been obtained. Such relationships are found to hold in systems that display fractal character, i.e. their topology is independent of the measurement scale. The fact that such relationships were not found in the initial stages of the work does not mean they do not exist, rather that they are very difficult to quantify. In pure percolation models the pressure is increased incrementally until the first possible instability is found during a single Monte Carlo time step. In this model, though, the pressure was held constant and the interface advance governed by the transformation, which was stochastically determined. As a result more interface smoothing was observed than in classical percolative systems. A future study could focus entirely on the determination of scaling laws, while focussing on only one or two model simulations.

Regardless of the potential for discovery of new scaling laws, the approach used (Weibull plots and process mapping) proved most useful for understanding the results

and presenting them in a format that Materials Science and Engineering professionals are most familiar with. They also serve as useful tools for experimentalists developing composites via these methods.

3 Algorithm Development

One of the most difficult aspects of computer modeling lies in the answer to the question, "How do I convince myself that this is right?" This is especially true in models involving complex algorithms like those based on percolation methods. Writing and testing code on the smallest lattices possible, without boundary conditions, was the most useful approach. The size of the lattice could then be sequentially increased and system boundaries added, and the errors discovered. This reduces the number of patches to the code that must be used in order to build upon it. The result is code that is termed "robust". Comparison to published work, such as the percolation analysis to determine critical contact angle completed here, is the best way to verify the validity of the results, short of breaking down hundreds of pages of code line-by-line with an acknowledged expert. Also, a baseline simulation is a useful tool for modifying the model so that the subsequently obtained simulations closely resemble the actual physical phenomena the model is designed for.

4 Physical versus Phenomenological Models

Much has been stated about the difference between physical and phenomenological models. Physical models like the one developed in this work remain

quite useful in analyzing empirical data obtained during process development, and in obtaining a more fundamental understanding of the physics and chemistry involved. It must be remembered that a computer model is successful only in the degree to which it predicts the results of an actual process. Incorporation of as much sound physics, chemistry, and mechanics as is possible is the goal, as it allows for confident extension of the insights learned from the current system to brand new systems. There is, as always, significant interplay between the two approaches.

Catalogue of the meniscus interactions operating in the Invasion Percolation growth algorithm employed. Each individual meniscus on the interface is referred to as an "arc", and each lattice element is referred to as a "disk". The instabilities, in their order of removal during the algorithm, are (1) touch; (2) overlap; (3) touch before burst; (4) overlap before burst; and (5) burst. Algorithm follows that of Cieplak and Robbins (1990).

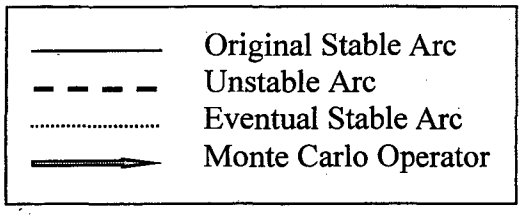

1. Touch: Arc contacts adjacent disk. Touch instabilities are removed by advancing the interface to the nearest disk on the lattice and creating two new arcs, each at the initial value of the contact angle.

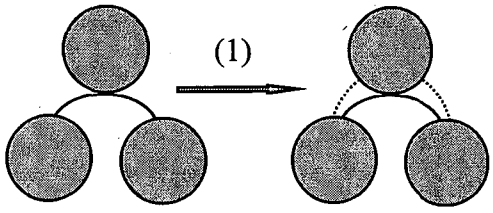

2a. Overlap: Adjacent menisci overlap on a disk. Overlap instabilities are removed by creating one new arc at the initial value of the contact angle. If the resulting arc is unstable, it is equilibrated according to the same hierarchy.

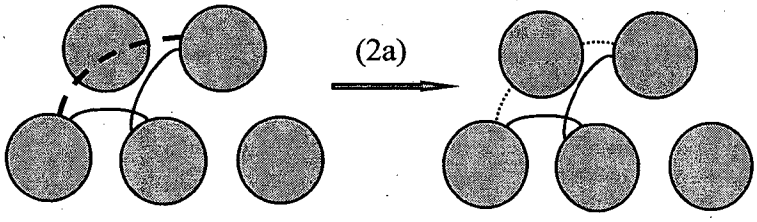

2b. Overlap: Adjacent menisci overlap in the pore space.

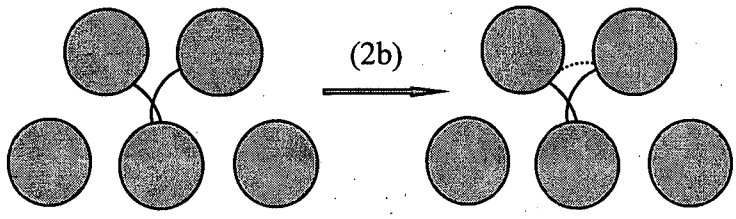

3. Touch before Burst: Arc is unstable at the given geometric configuration, but would contact an adjacent disk first. This type of burst instability is removed as a touch instability.

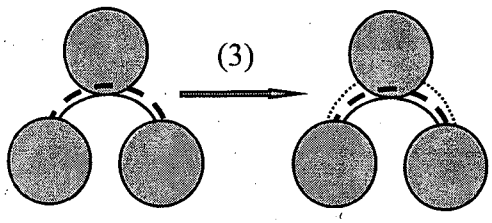

4. Overlap before Burst: Arc is unstable at the given geometric configuration, but would overlap an adjacent meniscus first. This type of burst instability is removed as an overlap instability.

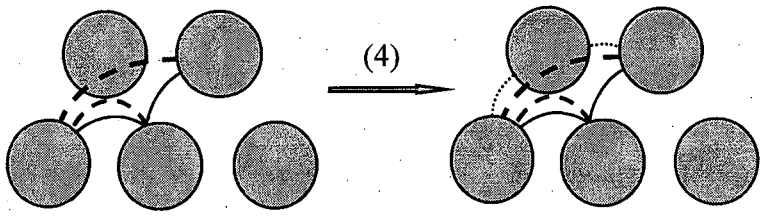

5. Burst: Arc is unstable at the current geometric configuration. No other interaction is possible. Burst instabilities are removed by advancing the interface to the nearest disk and creating two new arcs, each at the initial value of the contact angle.

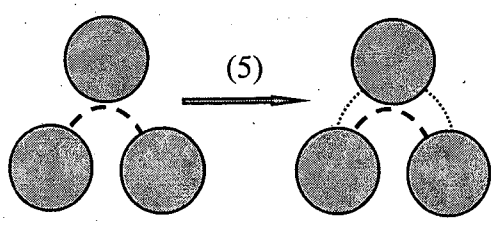

The mechanism for the computer model construction uses a cross-referencing data structures overlay. Three data structures, Disks, Arcs, and Pores, are overlain on a dual honeycomb lattice, with 2 pores associated with each disk lattice site. The data fields of each structure element can be accessed by a cross-referenced data structure via a memory pointer. For example, each arc on the interface points to each pore it has invaded. A pore is flagged partially filled when the arc has moved beyond it. A pore is flagged completely filled when its referenced arc undergoes an instability after the pore is partially filled. If the pore has not yet been invaded, it is flagged empty. A full description of the disk, arc, and pore status is required for the percolation statistics employed in the analysis of the output.

Arc[M] points to Disk [i][j] & Disk [i][j+1] & Pore_1 [i][j]
Arc[N] points to Disk [i+1][j] & Disk [i][j+1] & Pore_2 [i][j]

Disk [i][j+1] points to Arc[M] & Arc[N]

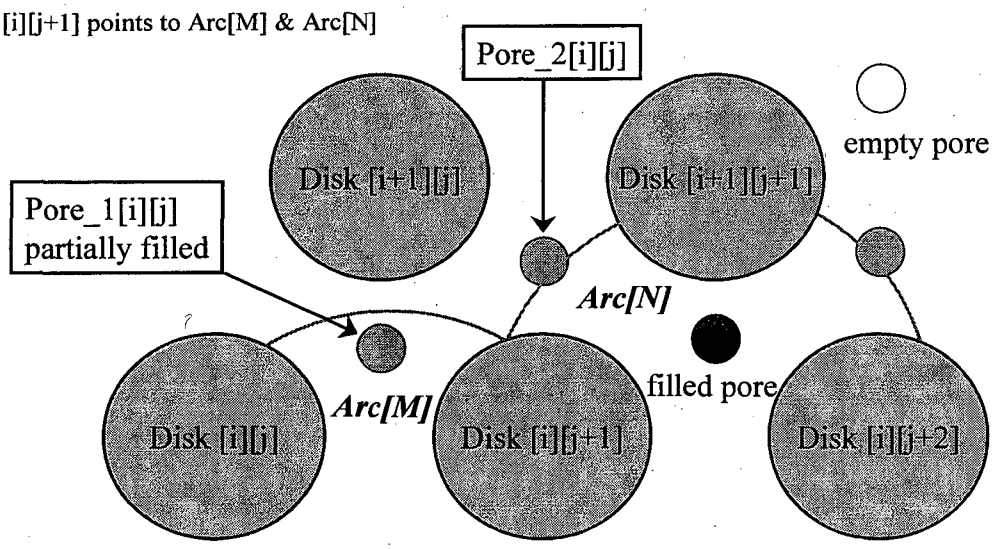

Flowchart for the Monte Carlo Invasion Percolation simulation, with interface transformation simulating chemical reaction kinetics, and formation of incompressible loops and reaction byproduct phase.

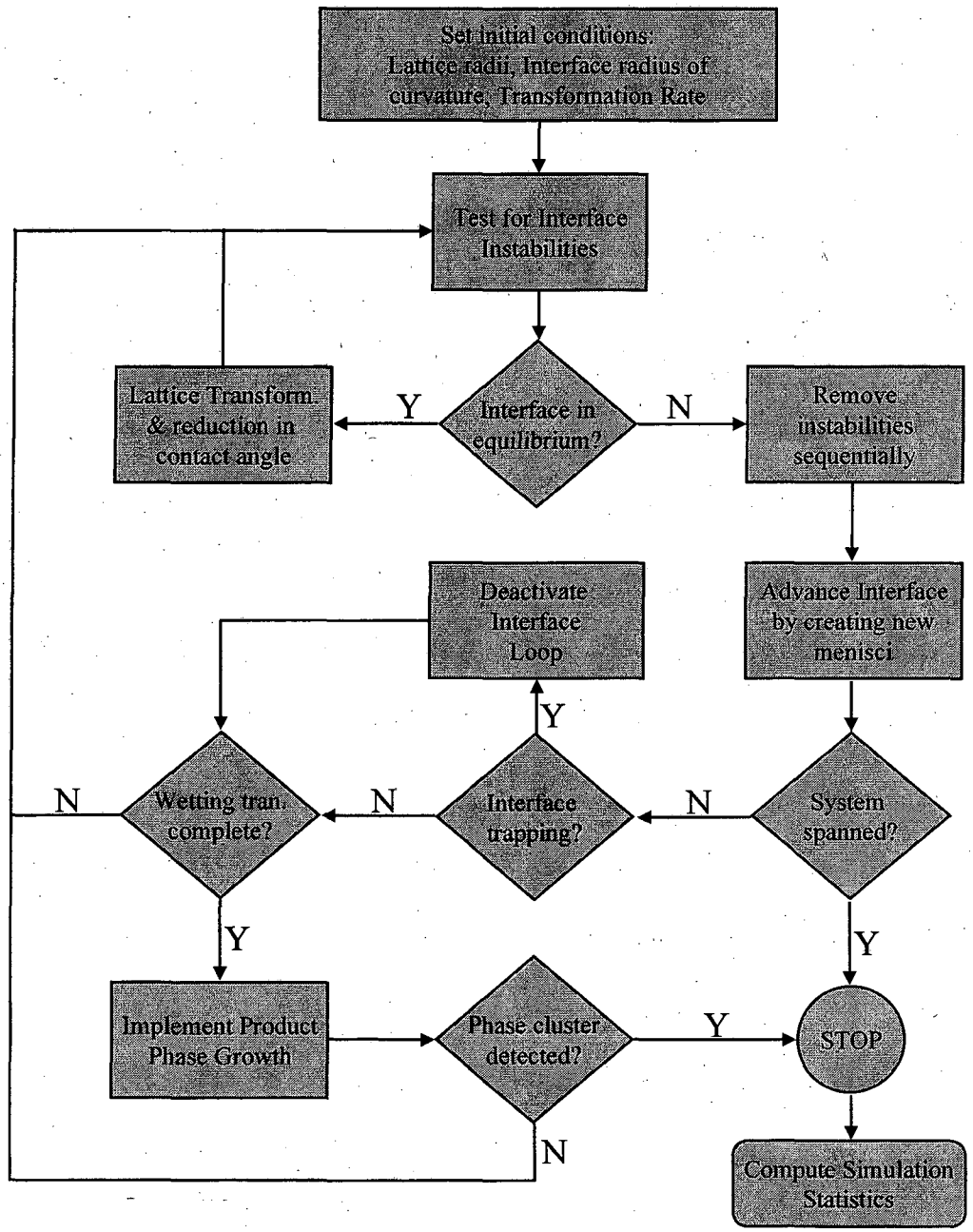

The development of failure probability from the flaw size distribution function proceeds as follows.[1] Assuming a sparse concentration of defects, such that all defects are non-interacting, let $p(a)$ be the probability of finding a flaw in the range $a \rightarrow a + da$ in one of M sub-volumes dV, with $M = 1/dV$. In a unit volume of material the expected number of flaws follows the distribution

$$q(a)dadV = p(a)da. \tag{1}$$

It is the probability, for samples of volume $V = NdV$, that the largest flaw lies in the range $a \rightarrow a + da$ (some critical parameter) that will determine the failure probability. From combinatorial theory, the probability of finding r defects in the total volume V is found by considering all possible distinguishable combinations of finding r sub-volumes with a defect in the range $a \rightarrow a + da$, and of finding N-r sub-volumes, which do not contain defects in this size range,

$$P_r(a)da = \frac{N!}{r!(N-r)!}[q(a)dadV]^r[1-q(a)dadV]^{N-r}. \tag{2}$$

In a sample of size V let $R(a)$ be the probability that zero defects lie in the range $a \rightarrow a + da$ and $S(a)$ be the probability that there are no defects of size greater than a. Then $Q(a, V)da = [1-R(a)]\ S(a)$ represents the probability that the largest defect lies in the range $a \rightarrow a + da$. $R(a)$ is simply one minus the sum over all N of the probabilities in equation (2)

$$R(a) = 1 - \sum_{r=1}^{N} P_r(a)da. \tag{3}$$

Upon expanding the first few terms of the summation this expression reduces to

$$R(a) = [1 - q(a)dadV]^N \cdot \tag{4}$$

With $V = NdV$

$$R(a) = \left[1 - \frac{q(a)da\{NdV\}}{N}\right]^N, \tag{5}$$

and the identity

$$\lim_{N\to\infty}\left[1 - \frac{x}{N}\right]^N = e^{-x} \tag{6}$$

one obtains,

$$R(a) = \exp[-Vq(a)da]. \tag{7}$$

The probability *S(a)* of finding no flaws greater than *a* can be found by discretizing space,

$$S(a) = R(a)R(a+da)R(a+2da)R(a+3da)\ldots \tag{8}$$

This can be rewritten using equation (7) as

$$S(a) = \exp\left[-V\sum_{r=0}^{\infty} q(a + r\delta a)\delta a\right]. \tag{9}$$

Combining (7) and (8) gives

$$Q(a)da = (1 - \exp[-Vq(a)da])\exp\left[-V\sum_{r=0}^{\infty} q(a + rda)da\right]. \tag{10}$$

Taking the limit as $\delta a \to 0$, by taking the Taylor series expansion of e^{-x} around zero, one obtains the function describing the maximum flaw size distribution

$$Q(a,V) = Vq(a)\exp\left[-V\int_a^{\infty} q(a')da'\right], \tag{11}$$

[1] see also Hunt, R.A., and McCartney, L.N. (1979)

with the dummy variable $a' = r_\delta a + a$. Integrating this expression gives the cumulative probability of finding at least one flaw in the volume V, where the exponential expression represents the probability that there are zero defects in volume V,

$$\int_0^\infty Q(a)da = 1 - \exp\left[-V\int_0^\infty q(a)da\right]. \tag{12}$$

If it is assumed that the sample of volume V will fail whenever a defect of a particular size occurs, and this defect is a function of the applied stress and geometric orientation, then for brittle materials a Griffith-type relation for the maximum allowable flaw size can be assumed, i.e.,

$$a_{\max} = X(\sigma) = \alpha/\sigma^2 \tag{13}$$

where α is a material constant, and $X(0) = \infty$ and $X(\infty) = 0$. Thus the probability distribution describing the failure probability at a stress in the range $\sigma \rightarrow \sigma + d\sigma$ because of a critical defect can be expressed as

$$P(\sigma,V)d\sigma = -X'(\sigma)Q(X(\sigma),V)d\sigma \tag{14}$$

where the negative sign is required since $X'(\sigma)$ is negative for all σ. Integrating this expression leads to the cumulative probability of failure at applied stress σ

$$\int_0^\infty P(\sigma,V)d\sigma = 1 - \exp\left(-V\int_0^\infty q(a)da\right). \tag{15}$$

It is clear from (15) that in a defect-free material there is a finite probability that samples will not fail at infinite applied stress. Assuming that a critical stress value exists, above which the ultimate strength of a defect-free material is exceeded, then a critical flaw size a_c corresponding to this critical stress exists such that $a_c = X(\sigma_c)$. Since flaw-initiated

failures will always occur at stresses less than σ_c, the distribution from $\sigma_c \rightarrow \infty$ is practically meaningless, and the expression in (15) can be rewritten as

$$\int_0^{\sigma_c} P(\sigma, V) d\sigma = 1 - \exp\left(-V \int_{a_c}^{\infty} q(a) da \right), \tag{16}$$

which is the desired result.

Ernest Orlando Lawrence Berkeley National Laboratory
One Cyclotron Road | Berkeley, California 94720

Prepared for the U.S. Department of Energy under Contract No. DE-AC03-76SF00098